Title

Exceptional stress-director coupling at the crack tip of a liquid crystal elastomer

Authors & Affiliations
Chen Wei,[1] Yu Zhou,[1] Benny Hsu,[1] Lihua Jin,[1,*]

[1]Department of Mechanical & Aerospace Engineering, University of California, Los Angeles, Los Angeles, CA, 90095
*To whom correspondence may be addressed. Email: lihuajin@seas.ucla.edu

Declaration of competing interests: Authors declare that they have no competing interests.

Data and materials availability: All data are available in the main text or the supplementary materials.

Abstract

A liquid crystal elastomer (LCE) is a special elastomer containing rod-like liquid crystals, which align in a certain direction, called the director. The director of a LCE can rotate under stress, resulting in large spontaneous strain and soft elastic behavior. This study unravels how the strong stress-director coupling in a monodomain LCE induces unique crack-tip fields and fracture behavior. Through stretching edge-cracked LCEs with various initial directors, we characterize the displacement and director fields theoretically and experimentally. The results reveal that the directors undergo significant and inhomogeneous rotation at the crack tips, leading to very different stress/strain distributions from traditional elastomers. Particularly, when the initial director is tilted to the loading direction, the stress/strain distributions are asymmetrical about the crack plane. Notably, we discover a domain wall forms along a certain polar angle at the crack tip, with opposite director rotation, and thereby shear strain, on the two sides of the domain wall. Moreover, LCEs with a tilted initial director to the loading exhibit much smaller crack openings and energy release rates than those of neo-Hookean materials, while LCEs with a parallel director exhibit higher values. We attribute these findings to a combined effect of bulk softening at the remote region and the formation of domains of opposite director rotation near the crack tip. This study provides an understanding of how the stress-director coupling of LCEs triggers their unique crack-tip fields, and insights into strategies to enhance the fracture properties of LCEs for future applications.

1 Introduction

Liquid crystal elastomers (LCEs) present a synergistic combination of cross-linked elastomers and rod-like liquid crystals (LCs), thereby exhibiting the hyperelasticity characteristics of elastomers and the unique properties associated with LCs. LCEs can be reversibly actuated by various external stimuli, such as heating (Naciri et al., 2003; Sawa et al., 2010; Schätzle et al., 1989), light irradiation (Finkelmann et al., 2001; Rogóż et al., 2016; Yu et al., 2003), magnetic fields (Kaiser et al., 2009; Schuhladen et al., 2014; Winkler et al., 2010), and electrical fields (Courty

et al., 2003; Fukunaga et al., 2008; Lehmann et al., 2001). Compared to other types of soft stimuli-response materials, LCEs have the advantages of high energy density, fast responses, safe operation and reversible actuation, facilitating broad applications including stimuli-responsive actuators (Lee et al., 2011; White et al., 2008; Yu and Ikeda, 2006) and soft robots (Ahn et al., 2019; Rogóż et al., 2016; Wang et al., 2018; White and Broer, 2015; Wu et al., 2023). Nevertheless, to achieve durable applications of LCEs, it is important to ensure no failure of LCEs under operation, thereby a careful consideration must be given to their fracture behavior.

However, the intricate stress-director coupling behavior in LCEs poses challenges in understanding the mechanism of their deformation and fracture. In a nematic LCE, the LC mesogens align around a particular orientation, with the average direction called the director, $\boldsymbol{d}$ (Stephen and Straley, 1974; Ericksen, 1991; Leslie, 1992), which can be identified by their uniaxial optical axis. The microscopic rotation of the director in response to external stimuli can lead to large macroscopic spontaneous deformation, or stress when the material is constrained. Conversely, mechanical stretch can also reorient the director toward the stretching direction (Küupfer and Finkelmann, 1994; Kundler and Finkelmann, 1995; Warner and Terentjev, 2007; Higaki et al., 2013; Mistry et al., 2018; He et al., 2020; Okamoto et al., 2021; Luo et al., 2022). Attributed to such a stress-director coupling effect, we expect significant and highly non-uniform director rotation near the crack tip of a LCE, which can dramatically influence its corresponding stress/strain distribution and fracture behavior.

Several studies have already demonstrated the pronounced impact of stress-director coupling on the fracture behavior of LCEs, which deviates considerably from that of traditional neo-Hookean materials. The reorientation of the director near the crack tip exerts remarkable influences on the fracture energy. Specifically, polydomain LCEs exhibit fracture energy of approximately 2808 J/m^2, monodomain LCEs under stretching parallel to the director display a reduced fracture energy of around 1000 J/m^2, while monodomain LCEs under perpendicular stretching exhibit a slightly lower fracture energy than the parallel case (Fan et al., 2016). The difference in the fracture energy among the different samples was attributed to the director rotation in polydomain LCEs and monodomain LCEs subjected to perpendicular stretching, although no further understanding of the numbers was provided. To investigate the director rotation due to stress concentration, a monodomain LCE sheet containing a circular or an elliptical hole subject to remote tension was analyzed by finite element method (FEM) (Jiang et al., 2023, 2021; Peng et al., 2023). It was found that when the initial director around the hole edge forms a tilted angle with the stretching, the stress concentration factor is lower than that in the parallel case, and reaches the minimum at the titled angle of $45°$. However, studying stress concentration solely is insufficient to fully comprehend the crack growth resistance in LCEs, and the intricated interplay of stress and the director around a sharp crack remains elusive. Moreover, the crack-tip fields of LCEs have not been experimentally characterized.

Characterizing the deformation fields around a crack tip under various loading plays an important role in validating crack-tip fields predicted computationally and analytically in highly deformable soft materials (Long et al., 2021; Lu et al., 2021; Qi et al., 2019). It becomes particularly crucial when it is challenging to develop an asymptotic solution for the stress/strain fields near a crack tip. Digital image correlation (DIC) has been proven effective in mapping the nonlinear deformation in the vicinity of a crack in highly deformable soft materials (Lin et al., 2014; Liu et al., 2019; Zhang et al., 2015). Zehnder et al. (Liu et al., 2019) utilized DIC to measure the strain distribution for a hydrogel specimen with an edge crack in the presence of large strain and strain gradients. In addition to DIC, the particle tracking method is an alternative method to probe inhomogeneous deformation fields. Long et al. (Lu et al., 2021; Qi et al., 2019) successfully utilized the particle tracking method to measure the deformation history near a crack in a rubber-like material subjected to tensile loading with different angles between the initial crack and the tension direction, equivalent to combined loading of tension and shear. Distinct from a common soft elastic material (Knowles and Sternberg, 1973; Long and Hui, 2015; Rivlin and Thomas, 1953), LCEs can have significant and highly inhomogeneous director rotation at the crack tip, which can induce a highly inhomogeneous spontaneous strain field. Characterizing the microscopic director field near a crack is essential to understanding the crack-tip and fracture behavior of LCEs.

In this paper, we analyze the fracture behavior of LCEs with a single-edge crack of length a subjected to remote strain ε^{∞}, as shown in Fig. 1(a). Motivated by the pronounced stress-director coupling of LCEs, we anticipate that the crack-tip fields and fracture behavior of LCEs are very different from those of traditional elastomers. On one hand, the highly inhomogeneous and concentrated stress at a crack tip can reorient the directors to different levels, inducing large and inhomogeneous spontaneous strain; on the other hand, different rotation capability of the directors around the crack tip gives rise to different levels of stress softening, influencing the stress distribution and energy release rate, and consequently leading to distinct crack opening shapes from traditional elastomers. Moreover, the angle between the initial director and the crack plane, θ_0, can dramatically vary the crack-tip fields and crack opening. Fig. 1(b) and 1(c) show two examples of the evolution of the director θ at different polar angles ϕ on the crack surface with respect to the remote strain ε^{∞} for different initial directors $\theta_0 = 90°$ and $30°$, and Fig. 1(a) illustrates the corresponding crack openings. In particular, when the initial director does not align with the remote strain, for instance $\theta_0 = 30°$, the adjacent directors exhibit opposite rotation around the crack tip, forming a domain wall, and the stress/strain field is highly asymmetric about the crack plane, as shown in Fig. 1(c). To demonstrate the unique crack-tip behavior, we simulate the stress, displacement and director fields in the vicinity of a sharp crack in LCEs with different initial directors, and subsequently evaluate their energy release rates. Moreover, experimental data capturing the deformation field by the DIC method and the director field by the crossed-polarized optical measurement will be acquired to validate the simulation results.

Through combining numerical modeling and experimental observations, we aim to gain a comprehensive understanding of the crack-tip fields and fracture behavior of LCEs. Notably, this study represents the first instance of observing the director and deformation fields in the vicinity of a crack in LCEs.

This paper is organized as follows. In Section 2, we introduce the detailed modeling and experimental methodology. In Section 3, we report the FEM analysis of the stress-director coupling around the crack-tip field. We present the experimental measurement of the director and displacement in Section 4. Section 5 shows fracture evaluation. Section 6 concludes the paper.

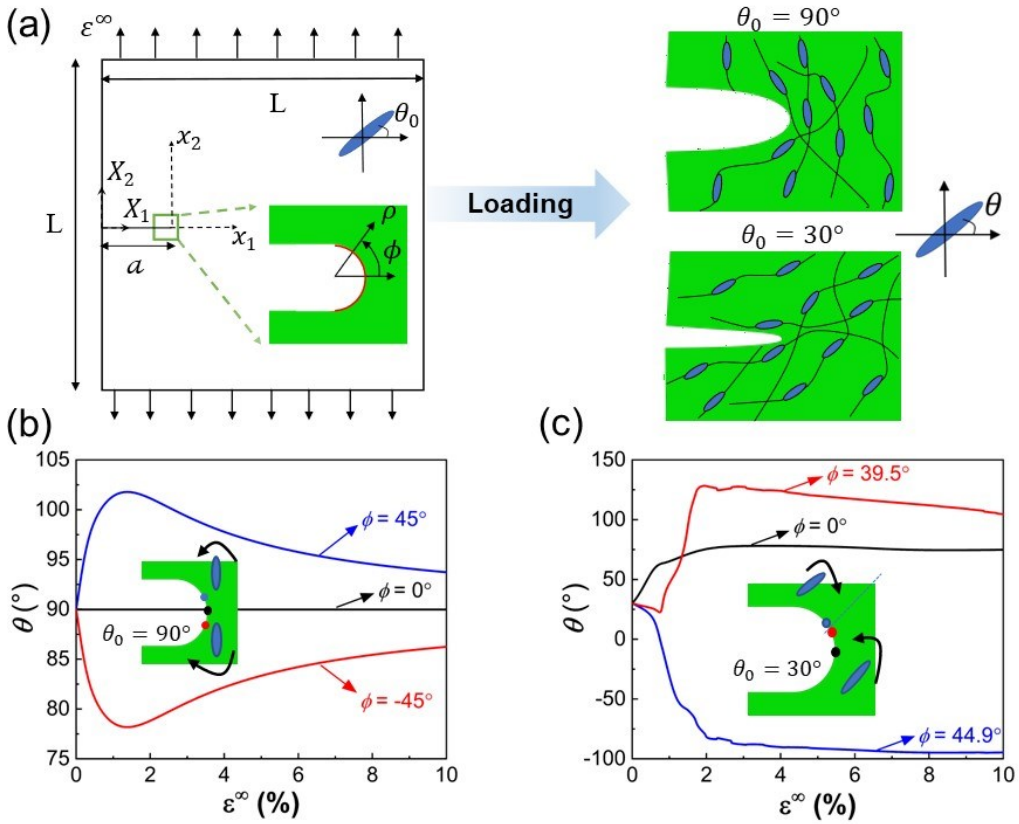

Fig. 1 Director rotation in edge-cracked LCEs under external tension. (a) Schematic illustration of an edge-cracked LCE sample subjected to remote strain ε^∞. Different initial directors, as shown for $\theta_0 = 90°$ and $\theta_0 = 30°$, lead to different crack openings due to director rotation. The director evolution at selected points on the crack surface as a function of the remote strain in the LCE with (b) $\theta_0 = 90°$ and (c) $\theta_0 = 30°$. Note that a polar coordinates (ρ, ϕ) and Cartesian coordinates in the reference configuration (X_1, X_2) and current configuration (x_1, x_2) are established; θ is defined as the angle between the director and X_1-axis.

2 FEM and experimental methodology

2.1 Constitutive model and FEM

To model the constitutive behavior of a LCE, we consider a material particle labeled by a position vector $\mathbf{X}$ in the stress-free reference configuration Ω_0 ($\mathbf{X} \in \Omega_0$) moves to the position $\mathbf{x}$ at time t in the current configuration Ω_c ($\mathbf{x} \in \Omega_c$). The deformation gradient is defined as $F_{iK} = \partial x_i(\mathbf{X}, t)/\partial X_K$. A unit vector $\boldsymbol{d}$ is used to describe the director orientation in the current configuration. Under the isothermal condition, the free energy density of nematic LCEs in the reference configuration is assumed (Warner and Terentjev, 2007; Zhang et al., 2019):

$$f_r(\boldsymbol{F}, \boldsymbol{d}, \nabla \boldsymbol{d}) = f_{el}(\boldsymbol{F}, \boldsymbol{d}) + f_{ss}(\boldsymbol{F}, \boldsymbol{d}) + f_{Frank}(\nabla \boldsymbol{d}) + f_c(\boldsymbol{d}). \quad (1)$$

The first term in Eq. (1),

$$f_{el}(\boldsymbol{F}, \boldsymbol{d}) = \mu(Tr(\boldsymbol{l_0 F l^{-1} F^T}) - 3 - 2ln(J))/2 + B(J-1)^2/2, \quad (2)$$

describes the entropic elasticity of the LCE network, which is also called the neo-classical free energy (Bladon et al., 1993), where μ is the shear modulus, B is the bulk modulus and $J = \det(\boldsymbol{F})$. The first part of the energy, $\mu Tr(\boldsymbol{l_0 F l^{-1} F^T})/2$, is a function of both $\boldsymbol{F}$ and $\boldsymbol{d}$, incoporating the coupling effect of the network deformation and the director rotation. $\boldsymbol{l}$ and $\boldsymbol{l_0}$ are the step length tensors in the current and reference configurations, respectively, $\boldsymbol{l} = (l_\parallel - l_\perp)\boldsymbol{d} \otimes \boldsymbol{d} + l_\perp \boldsymbol{I}$ and $\boldsymbol{l_0} = (l_\parallel^0 - l_\perp^0)\boldsymbol{d_0} \otimes \boldsymbol{d_0} + l_\perp^0 \boldsymbol{I}$, with $\boldsymbol{d_0}$ the director in the reference configuration. Since we consider the isothermal condition, the effective lengths along or perpendicular to the director in the current configuration ($l_\parallel$ and $l_\perp$) remain the same as those in the reference configuration ($l_\parallel^0$ and $l_\perp^0$), and we can denote the ratio $r = l_\parallel/l_\perp = l_\parallel^0/l_\perp^0$ as the anisotropy of the backbone. The second part, $B(J-1)^2/2$, is the energy associated with volume changes, with B the bulk modulus. We employ a large ratio of the bulk modulus to shear modulus, $B/\mu = 10^3$, to represent incompressibility. The second term in Eq. (1),

$$f_{ss}(\boldsymbol{F}, \boldsymbol{d}) = \mu Tr(\alpha(\boldsymbol{I} - \boldsymbol{d_0} \otimes \boldsymbol{d_0})\boldsymbol{F^T} \cdot \boldsymbol{d} \otimes \mathbf{d} \cdot \mathbf{F})/2 \quad (3)$$

describes the inevitable variation of the anisotropy r among chains, called the semi-soft elasticity (Verwey and Warner, 1997), with α a parameter describing the level of such fluctuation. We employ this term due to the occurrence of an obvious stress threshold before the stress plateau in the uniaxial stress-strain relation, as shown in our prior study (Wei et al., 2023). The third term in Eq. (1),

$$f_{Frank}(\nabla \boldsymbol{d}) = K \nabla \boldsymbol{d} : \nabla \boldsymbol{d}/2 \quad (4)$$

is a simplified form of the Frank energy, which describes energy associated with the spatial variation of the director (Frank, 1958). The incorporation of Frank energy in this study is because of the inhomogeneous rotation of the director, which leads to a non-zero spatial director derivative,

$\nabla \boldsymbol{d}$. The parameters of the Frank energy and network elasticity define a length scale, $\sqrt{K/\mu}$, which is typically on the order of 10 nm (Warner and Terentjev, 2007). The last term in Eq. (1),

$$f_c(\boldsymbol{d}) = \gamma_d(\boldsymbol{d}\cdot\boldsymbol{d} - 1) \tag{5}$$

enforces the constraint of the unit vector $\boldsymbol{d}$, $\boldsymbol{d}\cdot\boldsymbol{d} \equiv 1$, where γ_d is a Lagrange multiplier.

Consider the deformation of a LCE as an equilibrium isothermal process. The thermodynamic condition requires the variation of the free energy of the LCE over a small time increment should always equal the external power, $\int_{\Omega_0} \dot{f}_r dV = \dot{W}$, where $\dot{W} = \int_{\Omega_c} \boldsymbol{b}\cdot\dot{\boldsymbol{u}} dv + \int_{\Gamma_c} \boldsymbol{t}\cdot\dot{\boldsymbol{u}} da$ represents the power done by the body force $\boldsymbol{b}$ and surface traction $\boldsymbol{t}$ at the velocity $\dot{\boldsymbol{u}}$, respectively, in the current configuration, with Γ_c the prescribed traction boundary, and $\dot{} = \delta/\delta t$ in $\dot{f}_r$, $\dot{\boldsymbol{u}}$, $\dot{W}$ etc. represents a small variation over a small time increment. Using the relation $\dot{f}_r = \partial f_r/\partial \boldsymbol{F} : \dot{\boldsymbol{F}} + \partial f_r/\partial \boldsymbol{d} : \dot{\boldsymbol{d}} + \partial f_r/\partial \nabla \boldsymbol{d} : (\nabla \dot{\boldsymbol{d}})$, we can derive two governing equations related to $\dot{\boldsymbol{u}}$ and $\dot{\boldsymbol{d}}$,

$$div(\boldsymbol{\sigma}) + \boldsymbol{b} = \boldsymbol{0}, \tag{6}$$

$$J^{-1}\mu\left(\left(l_{\parallel}^{-1} - l_{\perp}^{-1}\right)\boldsymbol{F}\boldsymbol{l_0}\boldsymbol{F^T}\boldsymbol{d} + \alpha\boldsymbol{F}(\boldsymbol{I} - \boldsymbol{d_0}\otimes\boldsymbol{d_0})\boldsymbol{F^T}\boldsymbol{d}\right) \times \boldsymbol{d} - J^{-1}K\nabla^{\boldsymbol{2}}\boldsymbol{d}\times\boldsymbol{d} = \boldsymbol{0}, \tag{7}$$

where the Cauchy stress $\boldsymbol{\sigma}$ is

$$\boldsymbol{\sigma} = J^{-1}\mu(\boldsymbol{l}^{-1}\boldsymbol{F}\boldsymbol{l_0}\boldsymbol{F^T} + \alpha\boldsymbol{d}\otimes(\boldsymbol{I} - \boldsymbol{d_0}\otimes\boldsymbol{d_0})\boldsymbol{F^T}\boldsymbol{d}\cdot\boldsymbol{F^T} - \boldsymbol{I}) + 2B(J-1)\boldsymbol{I} - J^{-1}K(\nabla\boldsymbol{d})^T\nabla\boldsymbol{d}. \tag{8}$$

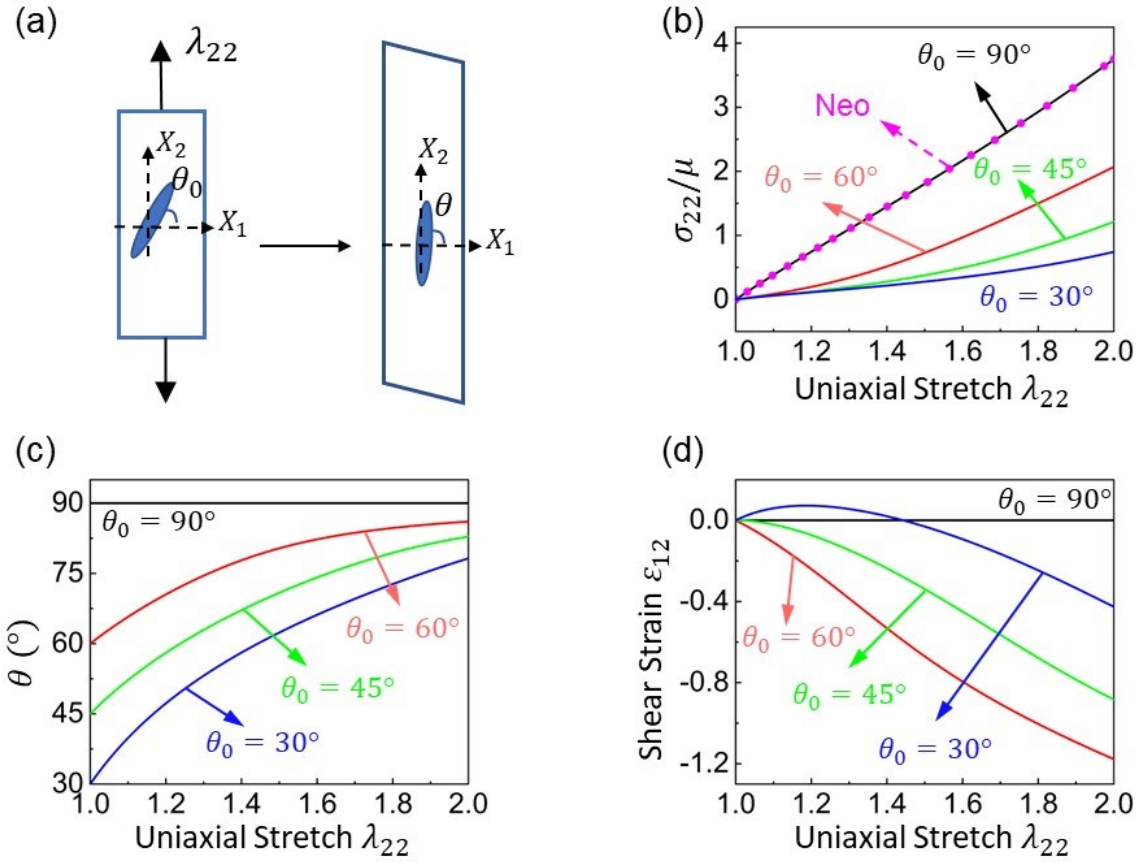

Fig. 2 Theoretical prediction of the uniaxial response of LCEs with different initial directors θ_0. (a) Schematic of the uniaxial stretch with the director rotation, θ. (b) Stress, (c) director, and (d) shear strain as functions of uniaxial stretch for different initial directors.

The constitutive model generally provides a comprehensive description of the properties exhibited by LCEs under uniaxial tension (Fig. 2(a)). It is observed that when the initial director aligns with the stretching direction ($\theta_0 = 90°$), the stress-stretch behavior resembles that of a neo-Hookean material (Fig. 2(b)) without director rotation and shear strain (Fig. 2(c) and 2(d)). In contrast, when the initial director is tilted away from the stretching direction ($\theta_0 = 60°, 45°, 30°$), stress softening occurs, accompanied by director reorientation and non-zero shear strain. The dependence of the stress, shear strain and director on the stretch predicted from the constitutive model agrees well with the experimental measurements at a slow loading rate reported by our previous work (Wei et al., 2023). Therefore, the current model is deemed capable of reasonably capturing the crack-tip fields of LCEs under quasistatic loading.

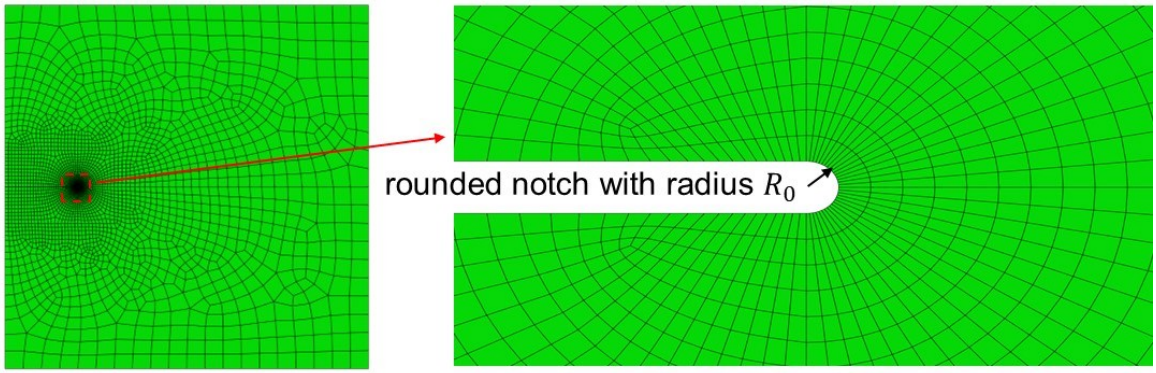

Fig. 3 Setup of the FEM model of a LCE specimen with a rounded notch tip with a radius $R_0/a = 5e-4$.

We further implemented the coupled director-displacement model into the commercial finite element software, ABAQUS, via a user element subroutine, UEL, detailed in Appendix A.2. To accommodate nearly incompressible solids and mitigate volumetric locking behavior, we implemented the F-bar method (Chester et al., 2015; de Souza Neto et al., 1996) and utilized 2D plane-strain 4-node linear quadrilateral elements in this study. We simulate a 2D rectangular LCE sample of an initial director θ_0 with an edge crack, as shown in Fig. 1(a). The top and bottom boundaries are controlled by a displacement in the X_2 direction, and fixed in the X_1 direction with a zero displacement, $u_1 = 0$. To prevent element distortion due to the strain concentration around the crack tip, a rounded notch is utilized, where the radius of the notch is $R_0/a = 5 \times 10^{-4}$ and the ratio of the crack length to the sample length is $a/L = 0.2$, with $L = 1\ mm$ (Fig. 3). We analyze fracture behavior when the crack opens much larger than the notch width so that the results are independent of the crack-tip shape (Knowles and Sternberg, 1974; Rice, 1968). To resolve the crack-tip fields and to ensure the element size in the vicinity of the crack tip comparable to $\sqrt{K/\mu}$, we set the size of the elements around the tip about 0.1 times of the notch size R_0, i.e. about $5e-5$ times of the crack length a, and $1e-5$ times of the model size L. Further reducing the element size around the crack tip has a limited impact on the results but leads to severe convergent issue. As we consider the plane strain condition, the director is described by the unit direction $\boldsymbol{d} = (cos(\theta), sin(\theta), 0)$ with θ the angle between the current director and the X_1-axis. The material properties are chosen as

$$\frac{B}{\mu} = 10^3, r = 5, \alpha = 0.1, \sqrt{\frac{K}{\mu}} = 10\ nm, \tag{9}$$

where the bulk modulus over the shear modulus is set large to represent incompressibility; both the material anisotropic parameter r, determined through a thermomechanical deformation test, and the semi-soft elasticity parameter α are based on our previous study (Wei et al., 2023); the

value of the Frank energy parameter with respect to shear modulus is estimated based on the previous report (Warner and Terentjev, 2007).

To ensure convergence of the simulations, small viscosity of the network and director rotation is added to the model. Moreover, the solution control parameters in ABAQUS are adjusted to allow an excessive number of increments and iterations to address the convergence issue. In particular, we set the maximum number of line search iteration to be 10. More details about the viscoelastic model and UEL implementation could be found in Appendix A.

2.2 Experimental methods

2.2.1 LCEs fabrication

In this study, the main-chain monodomain LCEs were synthesized via a two-stage thiol-acrylate Michael addition-photopolymerization (TAMAP) reaction (Saed et al., 2016). The crosslinker, pentaerythritol tetrakis(3-mercaptopropionate) (PETMP, 95%), and chain extender, 2,2-(ethylenedioxy) diethanethiol (EDDET, 95%), were obtained from Sigma-Aldrich and used as received. The diacrylate mesogen, 1,4-Bis-[4-(3-arcyloyoxypropyloxy) benzoyloxy]-2-methylbenzene (RM257, 95%), was purchased from Wilshire company. Dipropylamine (DPA, 98%) and (2-hydroxyethoxy)-2-methylpropiophenone (HHMP, 98%) were selected as the catalyst and photoinitiator, respectively. Toluene (98%) was used as the solvent for RM257. To prepare a sample, firstly, RM257 was fully dissolved in a vial with 60 wt% of toluene at 80 ℃. Then, PETMP, EDDET, HHMP, and DPA solution (DPA:toluene = 1:50) were poured into the solution and mixed using a vortex mixer for 60 s to obtain a uniform solution. The molar ratio of thiol functional groups between PETMP and EDDET was 15:85, corresponding to a ratio of 15 mol% PETMP. 3.87 mol% HHMP was a photo initiator used to enable the second-stage photopolymerization reaction. 1 mol% DPA with respect to the thiol functional group was used in this study. The solution was degassed for about 2 mins to remove all bubbles and then poured into a mold. Then the sample was cured at room temperature for 24 hours and put in an oven at 80 ℃ for another 24 hours to remove the toluene from the LCE sample. There would be an excess of 15 mol% acrylate groups for a second-stage photo-crosslinking reaction. In the second stage, the LCE sample was stretched uniaxially to 110% by a mechanical stretcher. The pre-stretched sample was exposed to UV light for 1 hour to photopolymerize the excess acrylate groups, forming a denser network. The thickness was measured at three locations by an electronic caliper, giving the average thickness over all specimens to be 0.45 ± 0.05 mm.

2.2.2 Tension tests

Rectangular strips with a width of 25 mm and length of 75 mm were cut out of a LCE sheet with angles $0°, 30°, 45°$, and $60°$ between the director and the longitudinal direction of the strips (Fig. 4(a)). The solid rod-like mesogen represents the director in the whole LCE sheet and the

titled red dashed line represents the cut LCE specimen with an initial director θ_0, which was measured by a protractor and further verified by the optical polariscopy method. In the specimens, 25 mm was left on each of the two ends for clamping and the middle region of 25 mm by 25 mm was used for fracture testing. We used a sharp blade to cut an edge crack of 5 mm in the middle of the height. The tension test was performed in an Instron universal testing machine (Model 5944) with a 50 N load cell. The specimens were uniaxially stretched up to 10% strain with steps of 0.5% of the gauge length imposed. In each step, the loading rate was 0.01%/s and we waited for another 5 mins to ensure the specimen reaches quasi-equilibrium before any measurements were taken. No crack propagation occurred during tension tests and all the specimens could be reused for multiple measurements.

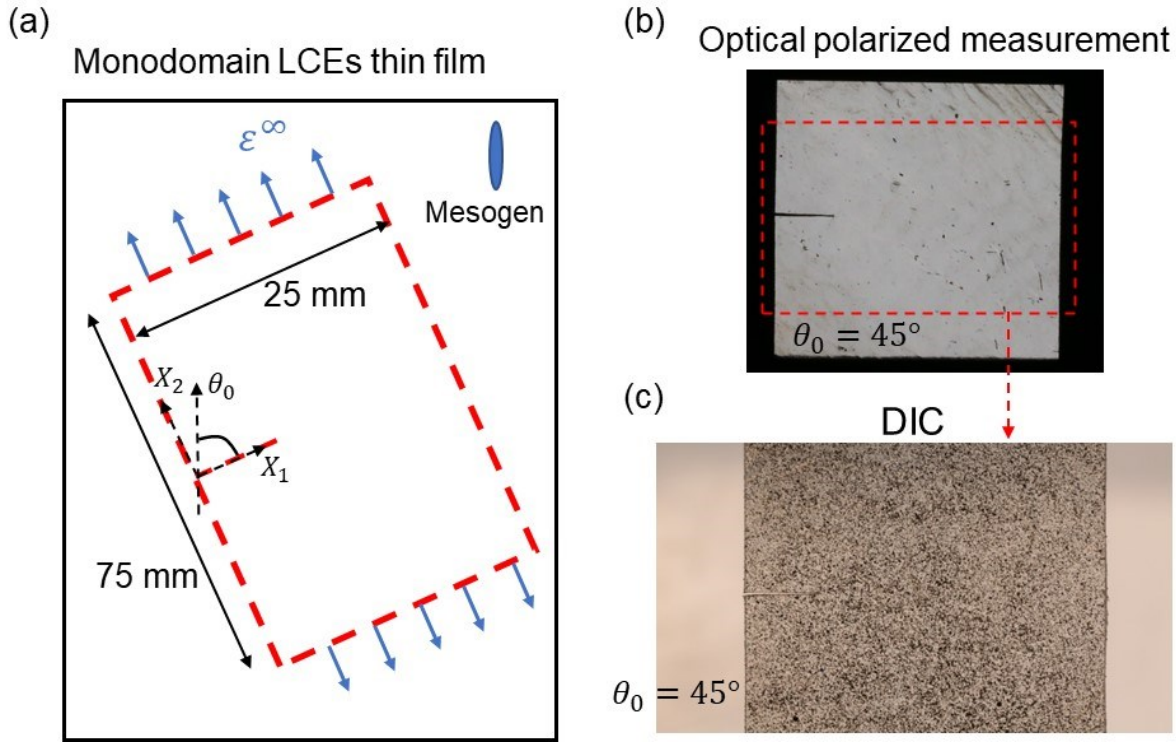

Fig. 4 (a) Schematic of a LCE specimen cut from a fabricated monodomain LCE thin film with the initial director angle θ_0 away from the transverse X_1 direction. (b) Image of a LCE specimen with initial director $\theta_0 = 45°$ at $\varphi = 0°$ and $\varepsilon^\infty = 0\%$ in an optical polarized measurement. (c) Image of the marked part of a LCE specimen in Fig. 4(b) with sprayed patterns for DIC tests.

2.2.3 Crossed-polarized optical measurements

Director rotation driven by stretching was characterized by crossed-polarized optical measurements. A light source, a polarizer, a specimen stretched by the Instron universal testing machine, an analyzer with the polarization perpendicular to the polarizer, and a camera were set up in the order (Supplementary Fig. S1). The appearance change of the specimen under uniaxial tension was recorded by a Canon ESO 6D DSLR camera along with a Canon 100mm F/2.8L macro lens.

The recorded images per 0.5% strain were used to measure the transmitted light intensity via ImageJ. We measured the transmitted light intensity for different orientations of the crossed-polarizers by rotating them every 10° from 0° to 90° to determine the director as a function of stretch. The recorded transmitted intensity I for different angles between the polarizer and the tension direction φ, can be fitted by the following equation to determine the director,

$$I = I_0 Sin^2\left(\frac{b\pi(\varphi-\theta)}{180}\right) + d, \quad (10)$$

where $I_0, b, \theta,$ and d are fitting parameters. In particular, the fitted parameter θ represents the current director. Fig. 4(b) shows an example of an LCE specimen during optical polarized measurement at $\varphi = 0°$ and $\varepsilon^{\infty} = 0\%$. At this moment, the specimen exhibits a uniform and brightest appearance. This observation validates the monodomain nature of the LCE specimen with the initial director $\theta_0 = 45°$.

2.2.4 DIC measurements

We use the 2D digital image correlation (DIC) method to measure displacement distributions. To generate a high-quality pattern, Koh-I-Noor Rapidraw ink, which dries fast and has a dark color, was sprayed using a Gocheer airbrush, which generates small droplets, at 30 psi with a 0.3 mm nozzle. The changes of speckle patterns under deformation were recorded per 1% strain by the same camera as mentioned above. To enhance the optical contrast, a whiteboard was used as a background, and a white LED light was shot on the sample. Fig. 4(c) shows an example of a sprayed sample with the initial director $\theta_0 = 45°$ at $\varepsilon^{\infty} = 0\%$. The images were then read by an open-source 2D DIC Matlab software, Ncorr (Blaber et al., 2015), to calculate the displacement field $\boldsymbol{u}$ around the crack tip in the marked region. Here, we set the three critical parameters that can affect the results as the following: subset radius as 25, subset spacing as 3, and strain radius as 20; more details are available in the instruction manual (http://www.ncorr.com/).

3 FEM analysis of the coupled stress-director effect on the crack-tip fields

We analyze the crack-tip fields of different initial directors $\theta_0 = 30°, 45°, 60°,$ and 90°. The FEM results have revealed highly inhomogeneous director rotation near the crack tip. When the initial director is parallel to the loading direction ($\theta_0 = 90°$; Fig. 1(b)), the director on the crack surface at $\phi = 45°$ rotates counter-clockwise and the director at $\phi = -45°$ rotates clockwise, where ϕ is the polar angle defined in the reference state, while the director remains unchanged at $\phi = 0°$. Intriguingly, when the initial director is inclined with respect to the loading direction ($\theta_0 = 30°$; Fig. 1(c)), the directors positioned in close proximity ($\phi = 39.5°$ and 44.9°) exhibit opposite rotation, i.e. the director at $\phi = 44.9°$ rotates clockwise, but the director at $\phi = 39.5°$ first rotates clockwise and then counter-clockwise, following a non-monotonic trend as the applied strain increases. Such unexpected and inhomogeneous director rotation triggers a question:

how does it influence fracture behavior in LCEs? To answer this question, we will next systematically investigate the stress, displacement and director fields, and subsequently the energy release rate.

3.1 Stress and strain distributions around a crack-tip

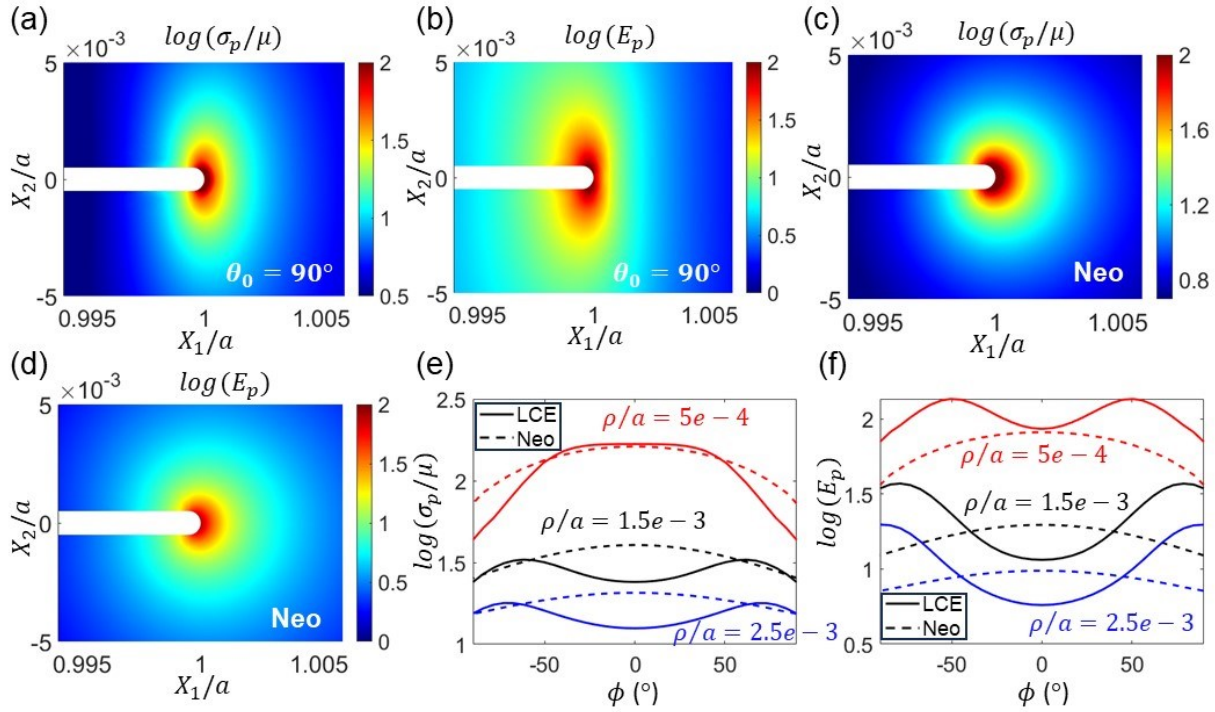

Fig. 5 FEM results of the stress and strain distributions around the crack tip at remote strain $\varepsilon^{\infty} = 10\%$. (a, c) Normalized maximum principal stress and (b, d) maximum principal Lagrangian strain around the crack tip in (a, b) a LCE with the initial director $\theta_0 = 90°$ and (c, d) a neo-Hookean material, respectively. The distribution of (e) normalized maximum principal Cauchy stress, and (f) maximum principal Lagrangian strain at different distances ρ/a around the crack tip at remote strain $\varepsilon^{\infty} = 10\%$ for a LCE with $\theta_0 = 90°$ and a neo-Hookean material. Note that on the crack surface, $\rho/a = 5e-4$.

To begin with, we consider a LCE with a parallel initial director to the remote tension direction ($\theta_0 = 90°$). We present the distributions of the normalized maximum principal Cauchy stress σ_p and the maximum principal Lagrangian strain E_p, where the Lagrangian strain is defined as $\boldsymbol{E} = (\boldsymbol{F}^T\boldsymbol{F} - \boldsymbol{I})/2$, in the region near the crack tip of size $0.01a$ under $\varepsilon^{\infty} = 10\%$ (Fig. 5(a) and 5(b)). We observe significant stress/strain concentration at the crack tip. The stress and strain are both symmetrically distributed about the X_1-axis with the contour lines exhibiting an elliptical shape, where a considerably smoother stress/strain gradient aligns in X_2 than that in X_1. LCEs present very different stress and strain distributions compared to those of neo-Hookean

materials, corresponding to $r = 1$, $\alpha = 0$ and $K = 0$ in Eqs. (6)(7), which show nearly concentric circular stress and strain contour lines (Fig. 5(c) and 5(d)). Further looking at the stress and strain distributions on the rounded notch surface, we find that while the locations of the maximum principal stress and strain are coincident at the polar angle $\phi = 0°$ in neo-Hookean materials, this is not the case in LCEs (Fig. 5(e) and 5(f)). Although the maximum stress occurs at $\phi = 0°$, consistent with that of neo-Hookean materials, strain peaks at two locations at around $\phi = \pm 50°$. Moreover, on the crack surface the maximum principal stress and strain in LCEs are both larger than those of neo-Hookean materials, which is consistent with the findings reported by Jiang et al. (Jiang et al., 2023) for a monodomain LCE sheet with an elliptical hole. It is worth noting that as indicated by the stress contour lines, in the region a little far from the rounded notch at $\rho/a = 1.5e-3$ and $2.5e-3$ (Fig. 5(e) and 5(f)), the location of the maximum principal stress is not at $\phi = 0°$ but shifts to around $\phi = 90°$ due to smoother reduction of stress concentration caused by director rotation that will be discussed later. The location of the maximum principal strain also shifts towards $\phi = 90°$.

When the initial director is tilted away from the stretching direction (Fig. 6 and Fig. 7), although the stress/strain is still highly concentrated at the crack tip, their distributions exhibit notable distinctions from the case of $\theta_0 = 90°$. Around the crack tip, the fields of stress and strain are no longer symmetrical about the X_1-axis, instead showing elliptic-like contour lines with a smoother gradient nearly along the initial director (Fig. 6). Moreover, the stress and strain values are significantly smaller than those of $\theta_0 = 90°$, and so is the normalized elastic energy density (Supplementary Fig. S2). For a LCE with $\theta_0 = 30°$, on the rounded notch surface, the peak maximum principal stress $\log(\sigma_p/\mu) = 1.26$ occurs at around $\phi = -22°$, while the peak maximum principal strain $\log(E_p) = 1.34$ occurs at around $\phi = 5°$ (Fig. 7(a) and 7(d)). The values are much smaller than those of neo-Hookean materials ($\log(\sigma_p/\mu) = 2.20$, and $\log(E_p) = 1.91$) and LCEs with $\theta_0 = 90°$ ($\log(\sigma_p/\mu) = 2.22$, and $\log(E_p) = 2.13$); see Fig. 5(e) and 5(f). Such asymmetrical stress and strain distributions lower than those of neo-Hookean materials are also found in other LCEs with tilted initial director $\theta_0 = 45°$ (Fig. 6(b, e) and Fig. 7(b, e)) and $60°$ (Fig. 6(c, f) and Fig. 7(c, f)). Similar to the case of $\theta_0 = 90°$, at the region a little far from the rounded notch at $\rho/a = 1.5e-3$ and $2.5e-3$, the location of the peak maximum principal stress/strain shifts towards the smoothest stress/strain gradient (Fig. 7).

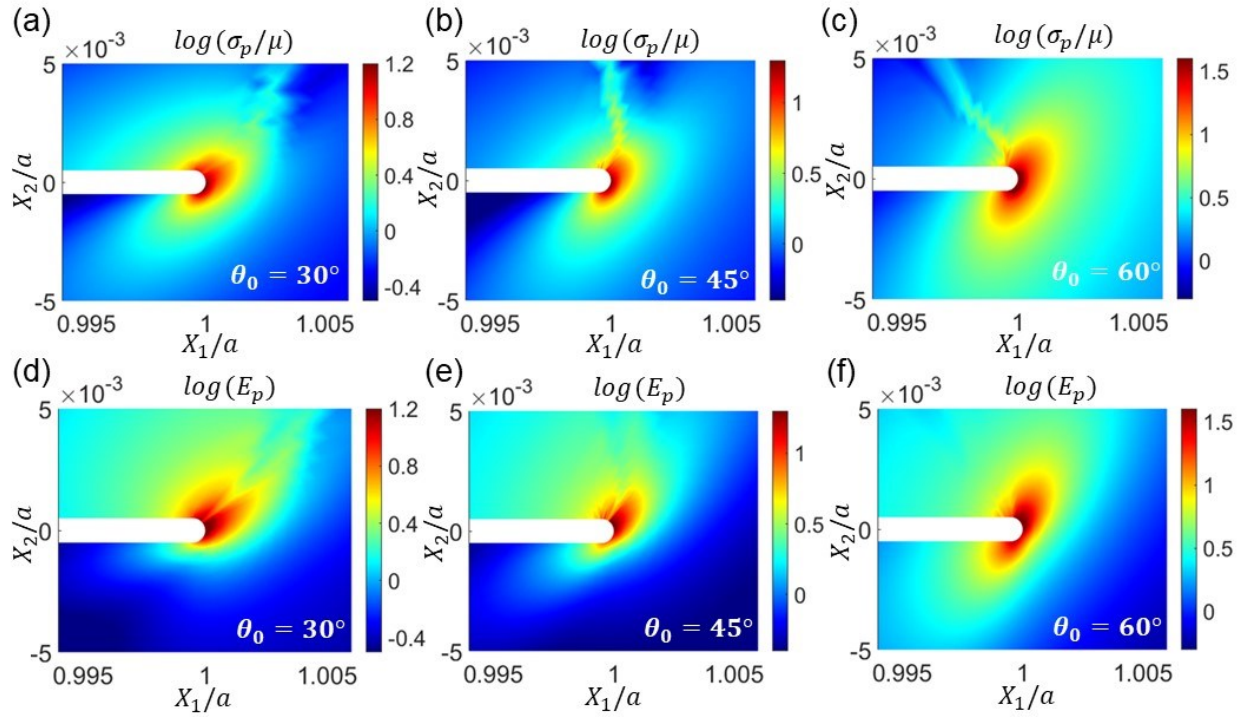

Fig. 6 FEM results of the stress and strain distributions around the crack tip at remote strain $\varepsilon^{\infty} = 10\%$. (a, b, c) Normalized maximum principal stress and (d, e, f) maximum principal Lagrangian strain around the crack tip in a LCE with the initial director (a, d) $\theta_0 = 30°$, (b, e) 45° and (c, f) 60°.

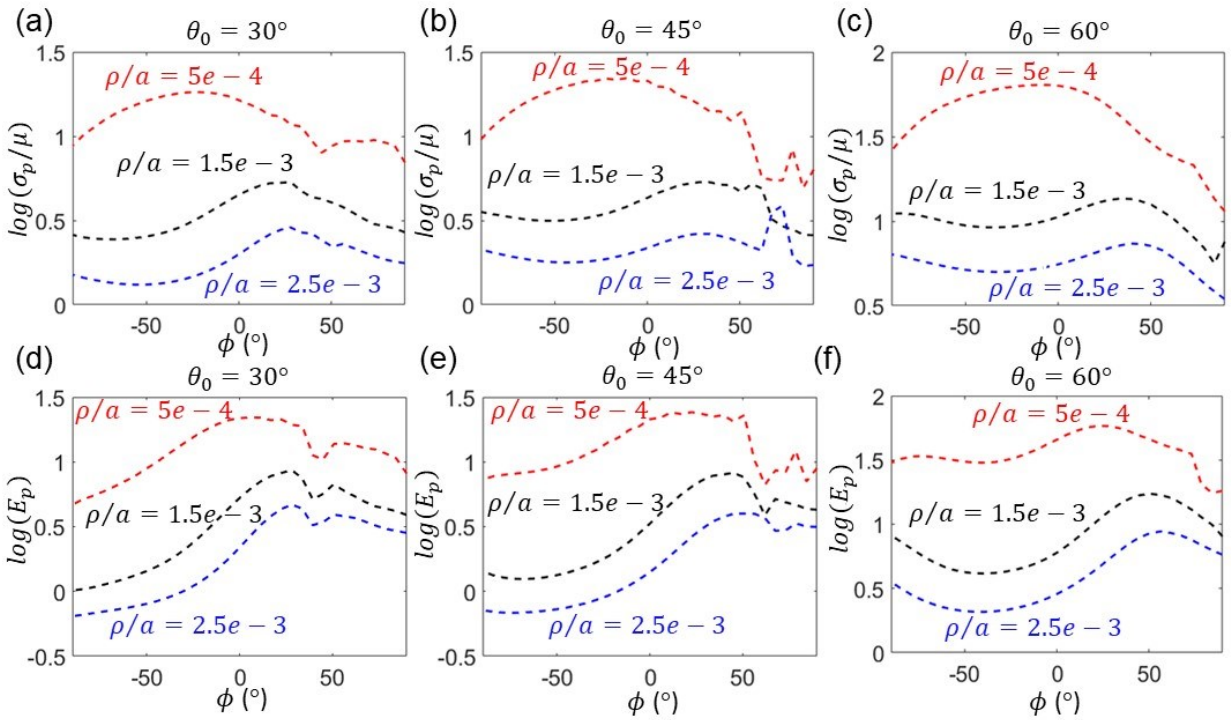

Fig. 7 FEM results of the stress and strain distributions at different distances ρ/a around the crack tip at remote strain $\varepsilon^{\infty} = 10\%$. (a, b, c) Normalized maximum principal stress, and (d, e, f) maximum principal Lagrangian strain at different distances ρ/a around the crack tip for a LCE with (a, d) $\theta_0 = 30°$, (b, e) $45°$ and (c, f) $60°$. Note that on the crack surface, $\rho/a = 5e-4$.

3.2 Director distribution around the crack-tip field

The observed unusual stress and strain distributions can be attributed to the inhomogeneous and high director rotation at the crack tip. For the LCE with $\theta_0 = 90°$ (Fig. 8(a)), the director at $\phi = 0°$ near the crack tip remains almost unrotated, as the director always aligns with the stretching in this region. In contrast, the director rotates clockwise at $\phi < 0°$ and counter-clockwise at $\phi > 0°$. Correspondingly, when we plot the director change, $\delta\theta = \theta - \theta_0$, we observe negative $\delta\theta$ at $\phi < 0°$ and positive $\delta\theta$ at $\phi > 0°$ (Fig. 8(b)). Further away from $\phi = 0°$, the director deviates more from $\theta = 90°$. Interestingly, non-monotonic director rotation with the applied strain is found around the crack surface. Fig. 8(b) shows the change of the director at $\varepsilon^{\infty} = 2\%$ is higher than that at $\varepsilon^{\infty} = 10\%$. To be specific, we select two representative points at $\phi = \pm 45°$ (Fig. 1(b)), where the director gradually deviates from $\theta_0 = 90°$, reaches the maximum rotation at $\varepsilon^{\infty} \approx 1.4\%$, and then gradually returns to the initial direction. We also plot the director change at different applied strains as shown in Supplementary Fig. S3(a). In general, the maximum director change, $\delta\theta = \theta - \theta_0$, is around $\pm 20°$ at $\phi = \pm 90°$ at $\varepsilon^{\infty} = 2\%$, but decreases to $\pm 8°$ at $\varepsilon^{\infty} = 10\%$.

Such non-monotonic director rotation can be explained based on the director alignment. Fig. 8(c) shows that at $\varepsilon^{\infty} = 10\%$ the director (red curve) in the vicinity of the crack surface aligns with the direction of the principal stress (blue crosses) and the tangent direction of the crack surface (green dots), while deviating from the direction of the principal Lagrangian strain (black curve) attributed to the spontaneous strain. The principal stress direction always aligns with the tangent direction of the crack surface, giving the absence of surface traction around the crack surface. When ϕ is larger or smaller than $0°$, the directions of the principal stress are larger or smaller than $90°$, respectively, and thereby the directors rotate toward the corresponding directions. However, the alignment becomes different when the applied strain is small; see Fig. 8(d) when $\varepsilon^{\infty} = 0.1\%$. The director (red curve) deviates much from the direction of the principal strain (black curve), principal stress (blue crosses) and the tangent direction of the crack surface (blue dots). At $-45° < \phi < 45°$, the directions of the principal stress and principal strain are coincident as the director undergoes limited rotation, while at $\phi < -45°$ and $\phi < 45°$, the directions of the principal stress and principal strain deviate more from each other as the director far from the crack tip undergoes more rotation, and the resultant higher spontaneous strain leads to the difference. Plotting these directions at different applied strain (Supplementary Fig. S4(a)) allows us to unravel that the non-monotonic director change is contributed by the two stages of director reorientation. At small ε^{∞} ($< \sim 2\%$), the director has not aligned with the direction of the

principal stress or tangent direction of the crack surface yet, and exhibits rapid and significant rotation towards the principal stress, so $|\delta\theta|$ increases with ε^{∞}; see the dashed curves in Supplementary Fig. S4(a) at $\varepsilon^{\infty} = 0.1\%$ (red curves) to 2% (blue curves). This substantial director rotation changes the stress and strain concentration around the notch. As ε^{∞} further increases ($>$ ~2%) after the director aligns with the principal stress direction, the crack is greatly opened and blunted, and the director rotates back towards 90°, following the deformation, so $|\delta\theta|$ decreases with ε^{∞}; see the dashed curves in Supplementary Fig. S4(a) at $\varepsilon^{\infty} = 2\%$ (blue curves) to 10% (black curves).

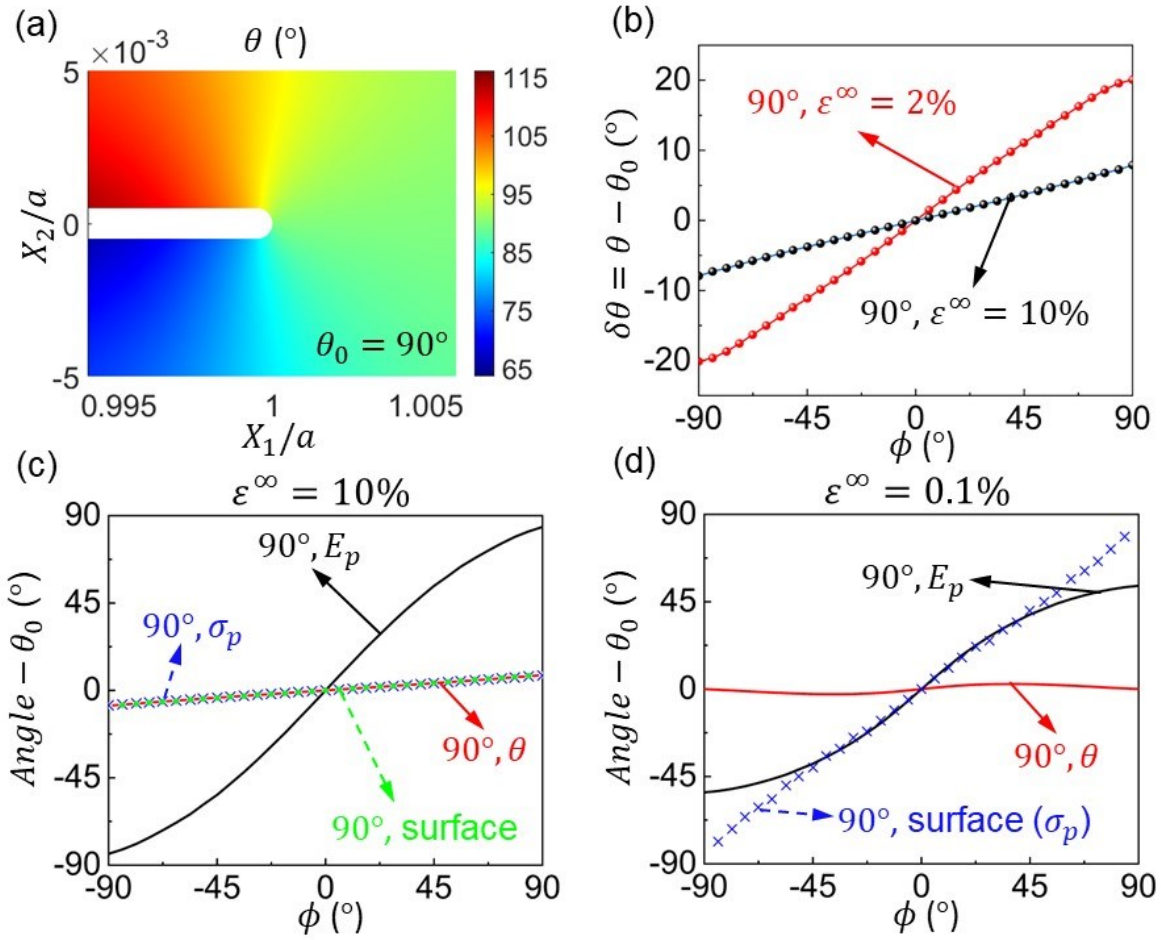

Fig. 8 FEM results of the director distributions around the crack tip for a LCE with $\theta_0 = 90°$. (a) Distributions of the director at remote strain $\varepsilon^{\infty} = 10\%$. (b) The change of director around the crack tip at remote strain $\varepsilon^{\infty} = 10\%$ and 2%. Relative directions of the director, maximum principal stress, maximum principal Lagrangian strain and the tangent direction of the crack opening surface with respect to the initial director $\theta_0 = 90°$ at (c) $\varepsilon^{\infty} = 10\%$, and (d) $\varepsilon^{\infty} = 0.1\%$ on the crack surface.

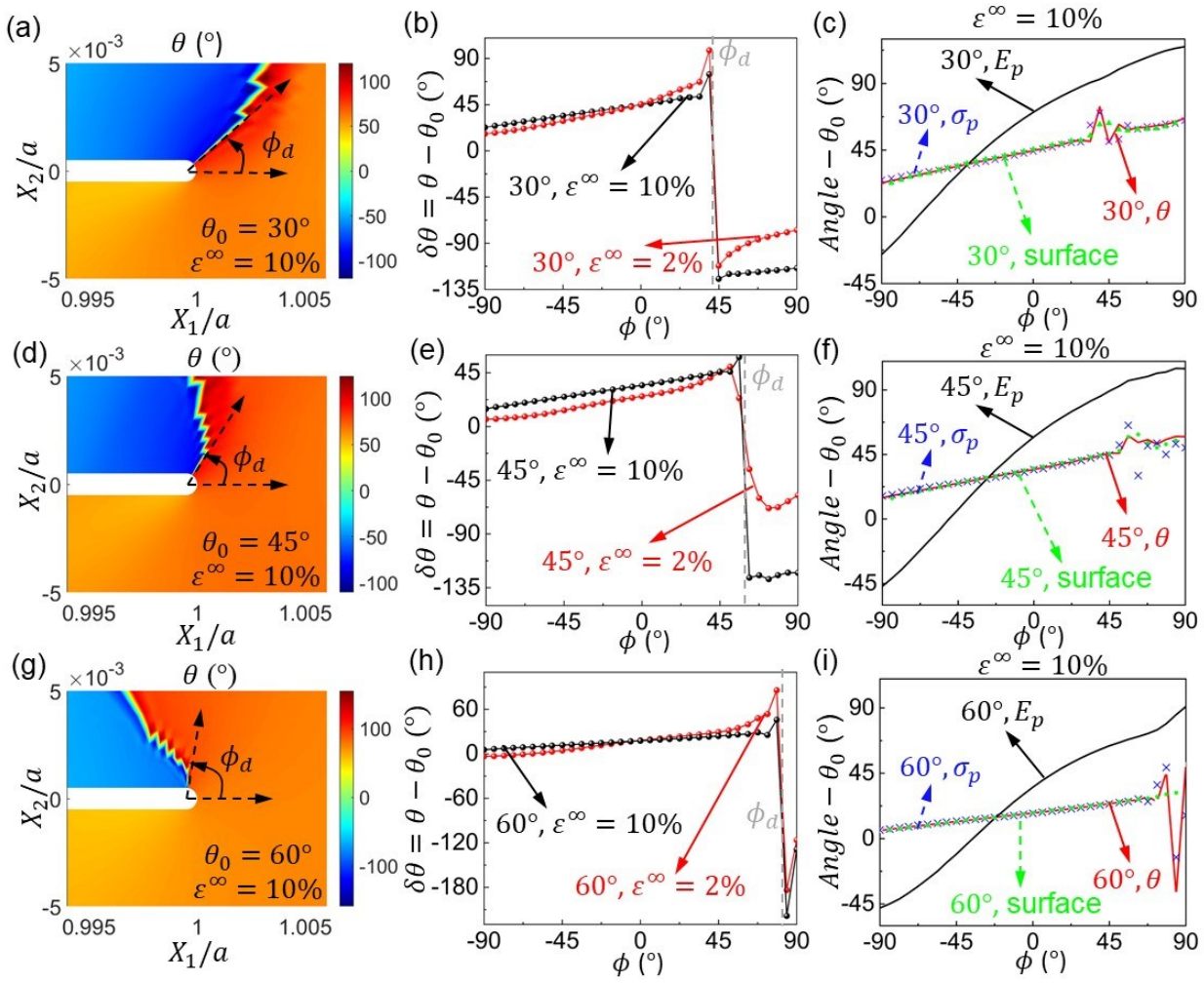

Fig. 9 FEM results of the director distributions around the crack tip for a LCE with $\theta_0 = 30°$, 45° and 60°. Director fields around the crack tip in LCEs with the initial director (a) $\theta_0 = 30°$, (d) $\theta_0 = 45°$, and (g) $\theta_0 = 60°$ at $\varepsilon^\infty = 10\%$ in the reference configuration. Changes of director on the crack surface in LCEs with the initial director (b) $\theta_0 = 30°$, (e) 45°, and (h) 60° at $\varepsilon^\infty =$ 2% and 10%. Relative directions of the director, maximum principal stress, maximum principal Lagrangian strain and the tangent direction of the crack opening surface with respect to the initial director θ_0 for LCEs with (c) $\theta_0 = 30°$, (f) 45°, and (i) 60° on the crack surface at $\varepsilon^\infty = 10\%$. Note that in Fig. 9(c,f,i) the clockwise director rotation at one side of the domain wall is added by 180° due to the symmetry of the director.

For the LCEs with $\theta_0 = 30°$, 45° and 60°, we observe a domain wall at a specific angle $\phi = \phi_d > 0°$, where the adjacent director rotates to opposite directions — clockwise at $\phi > \phi_d$ and counter-clockwise at $\phi < \phi_d$, as depicted in Fig. 9. As a result, near the domain wall, a sharp jump of the director is observed (Fig. 9(b,e,h) and Supplementary Fig. S3(b-d)). The angle ϕ_d monotonically increases with θ_0; when $\theta_0 = 30°$, 45° and 60°, ϕ_d equals around 42°, 53°, and

81.5°, respectively, at $\varepsilon^{\infty} = 10\%$ (Fig. 9(a,d,g)). Note that in Fig. 9(c,f,i), the clockwise director rotation at one side of the domain wall at $\varepsilon^{\infty} = 10\%$ is added by 180° due to the symmetry of the director. The formation of the domain wall is caused by the nearly perpendicular director to the principal stress direction at ϕ_d, and consequently the directors on the two sides of the domain wall undergo large rotations toward each other to nearly align with the crack surface. Similar formation of domain walls was reported for monodomain LCEs under uniaxial perpendicular stretching, where strip domains, i.e. adjacent domains with directors rotating in opposite directions, are shown to reduce the overall elastic energy (Verwey et al., 1996). The director around the crack tip also undergoes two stages of reorientation as in the case of $\theta_0 = 90°$ (Fig. 9(b,e,h), Fig. 9(c,f,i) and Supplementary Fig. S4(b-d)): at the beginning, the director did not align with the principal stress direction or the tangent direction of the crack surface, and the director exhibits considerable rotation until it aligns with the principal stress at $\varepsilon^{\infty} = \sim 2\%$; see the dashed curves in Supplementary Fig. S4(b-d) from $\varepsilon^{\infty} = 0.1\%$ (red curves) to 2% (blue curves). As the remote strain increases to $\varepsilon^{\infty} > \sim 2\%$, the crack tip surface is significantly blunted and opened to nearly 90°, and thereby, the director rotates more slowly following the deformation and approaches 90°; see the dashed curves in Supplementary Fig. S4(b-d) from $\varepsilon^{\infty} = 2\%$ (blue curves) to 10% (black curves). Therefore, for LCEs with tilted initial directors, non-monotonic director rotation only occurs at approximately $0 < \phi < \phi_d$. For example, at $\phi = 39.5°$ for the LCE with $\theta_0 = 30°$, the director angle increases to around $\theta = 127°$ at $\varepsilon^{\infty} = 2\%$, but decreases to around 104° at $\varepsilon^{\infty} = 10\%$ (Fig. 1(c)).

3.3 Elucidating the effect of stress-director coupling

Understanding the inhomogeneous director field at the crack tip can shed further light to the stress and strain distributions. The director rotation for the LCE with $\theta_0 = 90°$ induces compressive spontaneous strain normal to the crack surface, consequently facilitating the crack opening. The director rotation also causes stress softening, resulting in a lower stress/strain gradient towards $\phi = \pm 90°$, and thereby, the elliptical-shaped stress/strain contour lines; see Fig. 5(a) and 5(b). To explicitly compute the spontaneous strain, we define the spontaneous Lagrangian strain $\boldsymbol{E_s}$ as the difference between the Lagrangian strain and elastic Lagrangian strain, $\boldsymbol{E}_s = \boldsymbol{E} - \boldsymbol{E}_{elas}$, where $\boldsymbol{E}_{elas} = (\boldsymbol{R^T B}_{elas}\boldsymbol{R} - \boldsymbol{I})/2$ and $\boldsymbol{B}_{elas} := \boldsymbol{l}^{-1}\boldsymbol{F l}_r\boldsymbol{F^T} + \alpha \boldsymbol{d} \otimes (\boldsymbol{I} - \boldsymbol{d_0} \otimes \boldsymbol{d_0})\boldsymbol{F^T d} \cdot \boldsymbol{F^T}$, and $\boldsymbol{R}$ is the rigid rotation matrix in the polar decomposition of the deformation gradient $\boldsymbol{F} = \boldsymbol{RU}$ (Jiang et al., 2021). The principal spontaneous Lagrangian strain E_{sp} for the LCE with $\theta_0 = 90°$ distributes symmetrically about $\phi = 0°$ (Supplementary Fig. S5(a)), consistent with the director changes - the more director rotation indicates more spontaneous strain.

Similarly, for LCEs with tilted directors, the significant director rotation induces large spontaneous strain, and causes sharp changes in stress and strain at ϕ_d (Fig. 6). In particular, when ε^{∞} is small, the directors rotate in the opposite direction on the two sides of the domain wall, so the shear strain is opposite, consequently resulting in sharp shape changes on the crack surface; see

the significant difference of the adjacent directors (represented by blue and red solid cylinders) in Fig. 10(a). On the other hand, when ε^{∞} is large ($> \sim 2\%$), the director difference on the two sides of the domain wall gets close to 180°, and the director distribution becomes almost continuous across the domain wall again because the directors $\boldsymbol{d} = -\boldsymbol{d}$ are symmetric (Fig. 10(b)). Therefore, we added 180° to the clockwise director rotation when the director angle difference is more than 150° in Fig. 9(c,f,i). As a result, when the remote strain is high, the crack opening surface becomes smooth again. Similar to the case of $\theta_0 = 90°$, the spontaneous strain also causes stress softening, resulting in similar elliptical-shaped stress/strain contour lines, but with the axis of the smoother gradient aligning around the direction of $\phi = \phi_d$ (Fig. 6). Due to the much higher director rotation and softening effect, the stress/strain concentration for a tilted θ_0 is much lower than that of $\theta_0 = 90°$.

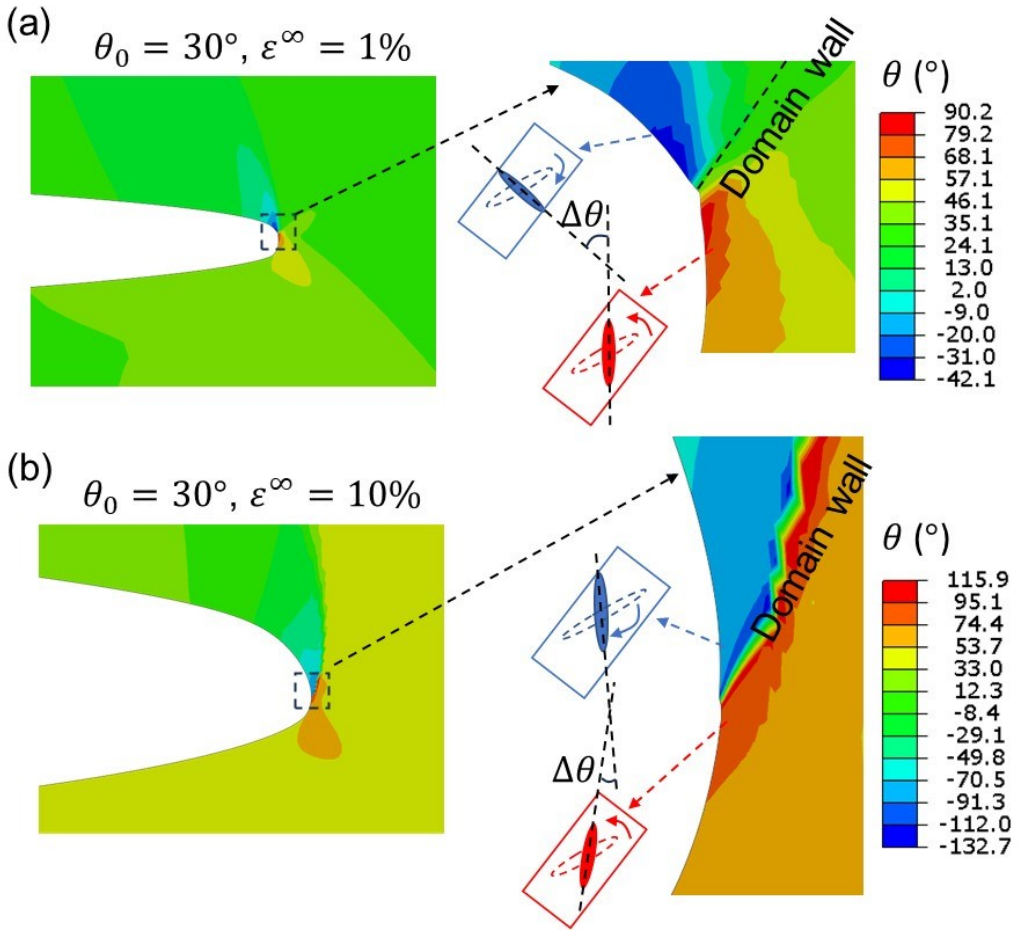

Fig. 10 FEM results of the director distribution around the crack tip showing the formation of a domain wall. (a) Distribution of the director near the domain wall for the LCE with $\theta_0 = 30°$ at (a) $\varepsilon^{\infty} = 1\%$ and (b) $\varepsilon^{\infty} = 10\%$, along with schematics showing the directors adjacent to the domain wall before (dashed hollow cylinders) and after (solid cylinders) deformation. An obvious crack surface discontinuity is observed at $\varepsilon^{\infty} = 1\%$, accompanied by a large difference in

the director alignment across the domain wall, $\Delta\theta$, while the discontinuity is reduced with the difference almost vanishing at $\varepsilon^{\infty} = 10\%$.

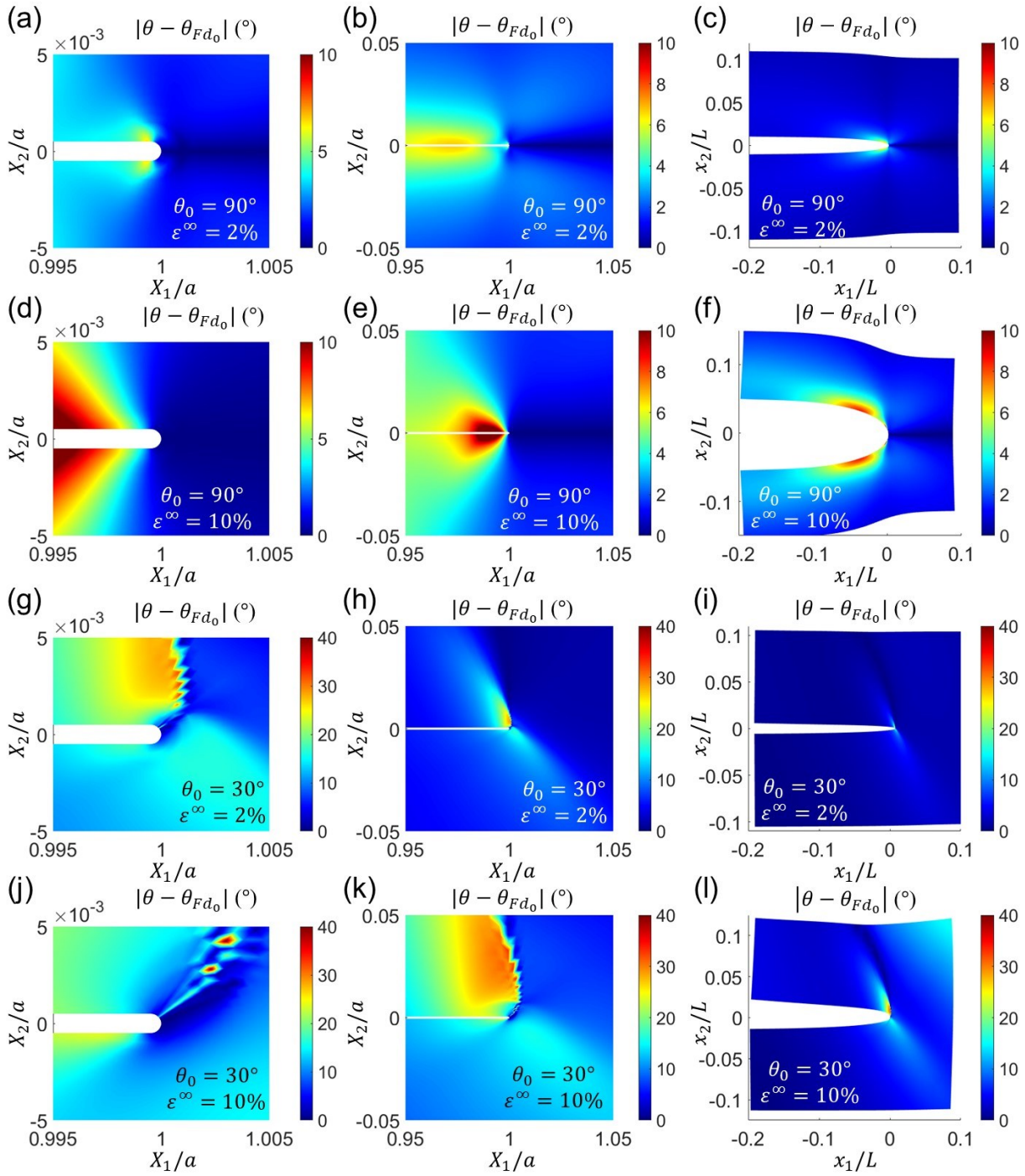

Fig. 11 FEM simulation results of the angle difference $|\theta - \theta_{Fd_0}|$. θ_{Fd_0} is defined as $(\cos(\theta_{Fd_0}), \sin(\theta_{Fd_0}), 0) = \boldsymbol{Fd_0}/|\boldsymbol{Fd_0}|$, denoting the portion of the director rotation following

the deformation gradient. The angle difference $\left|\theta - \theta_{Fd_0}\right|$ for LCEs with (a-f) $\theta_0 = 90°$ and (g-l) $\theta_0 = 30°$ at (a-c, g-i) $\varepsilon^\infty = 2\%$ and (d-f, j-k) $\varepsilon^\infty = 10\%$, respectively, shown in different regions.

Such strong stress-director coupling in LCEs results in their director rotation distinct from the realignment of fibers in fiber-reinforced elastomer (Gasser et al., 2005). We denote the portion of director rotation simply following the deformation gradient, similar to fiber realignment, as $\left(\cos\left(\theta_{Fd_0}\right), \sin\left(\theta_{Fd_0}\right), 0\right) = \boldsymbol{Fd_0}/|\boldsymbol{Fd_0}|$, and plot the angle difference $\left|\theta - \theta_{Fd_0}\right|$ in Fig. 11. Although the difference is relatively small in remote regions due to limited deformation, and at the crack tip, where exceptionally large deformation prevails, the difference becomes considerably pronounced around and behind the crack tip, see Fig. 11(a,d,g,j) and Fig. 11(b,e,h,k). This difference becomes increasingly obvious as the applied strain grows from 2% to 10%. In contrast to the condition in the remote and crack tip areas, the large angle difference in these regions is attributed to the moderate deformation the material experiences. Consequently, the directors in these regions still need to undergo further rotation in order to align with the principal stress direction. The difference between the director rotation and fiber reorientation indicates the distinctively strong stress-director coupling in LCEs.

4 Experimental measurement of director and displacement

4.1 Director measurement via the crossed-polarized optical measurement

To validate our simulations, we fabricated LCEs and characterized the director rotation driven by slow stretching sufficiently close to equilibrium. The crossed-polarized optical measurement was employed to measure the transmitted light intensity, which was used to calculate the director; see Section 2.2. More details about the experimental method were elaborated in our previous study (Wei et al., 2023). Fig. 12 shows the measured director contour from the experiment in comparison with the corresponding FEM simulation results at $\varepsilon^\infty = 10\%$. In general, the director near the crack tip exhibits a significantly larger rotation compared to the remote regions.

The experimental observations confirm the occurrence of opposite director rotation near the crack tip. In the case of a LCE with $\theta_0 = 90°$ (Fig. 12(a) and 12(b)), near the crack tip, the director rotates clockwise at $\phi < 0°$ and counter-clockwise at $\phi > 0°$; far behind the crack tip, the director rotates counter-clockwise at $\phi < 0°$ and clockwise at $\phi > 0°$; in remote regions, the director remains close to 90° due to the parallel loading. For the cases of LCEs with $\theta_0 = 30°$, 45° and 60° (Fig. 12(c-h)), a sharp transition in director is observed near the crack tip at a critical ϕ angle, verifying the existence of a domain wall. When ϕ is larger than the critical angle, the director rotates clockwise, while when ϕ is smaller than the critical angle, the director rotates counter-clockwise, contrary to the behavior exhibited by LCEs with $\theta_0 = 90°$. Comparison between the optical measurement and simulations reveals a high level of agreement of the director

near the crack tip. The simulations show higher maximum values, which is attributed to the different resolutions of the experimental and simulation tools, i.e. the optical measurement has a resolution of ~0.047 mm/pixel, whereas the element size at the crack tip in the simulations is around 0.0025 mm. Therefore, our simulations provide results in closer proximity to the tip, naturally yielding higher maximum values.

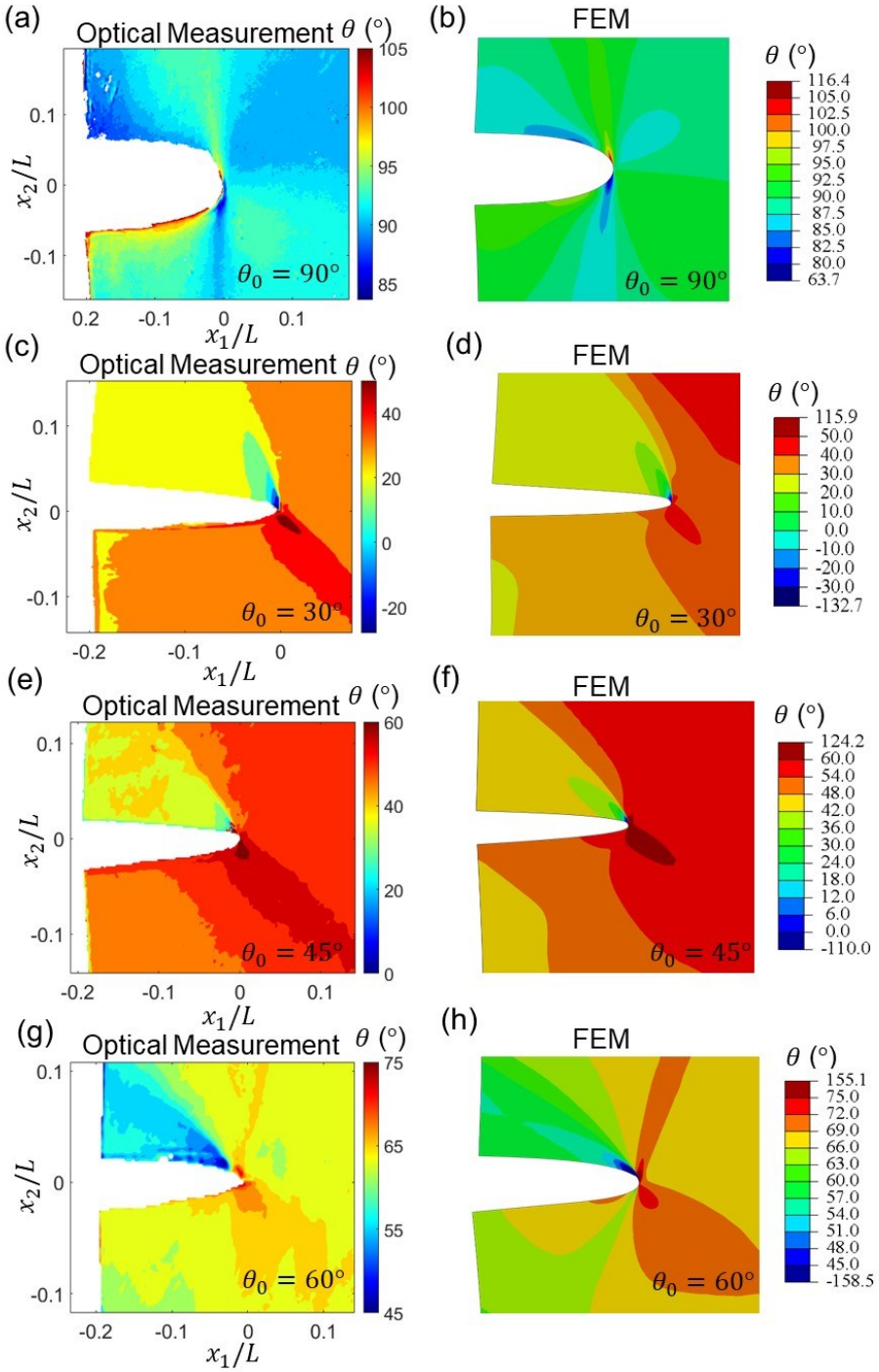

Fig. 12 Comparing the director fields obtained from the crossed-polarized optical measurements and FEM at $\varepsilon^{\infty} = 10\%$. Director distributions (a, c, e, g) measured by the crossed-polarized optical measurement and (b, d, f, h) calculated by FEM for LCEs with (a, b) $\theta_0 = 90°$ (c, d) 30°, (e, f) 45°, and (g, h) 60°, respectively.

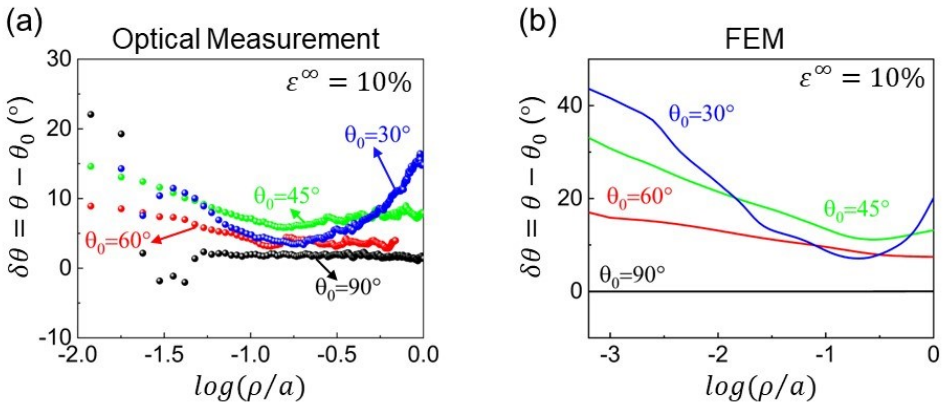

Fig. 13 Director distributions ahead of the crack tip for LCEs with $\theta_0 = 90°, 60°, 45°, 30°$ obtained by (a) optical measurement and (b) FEM under $\varepsilon^{\infty} = 10\%$.

We also find non-monotonic director distributions along the distance from the crack tip, ρ/a, at $\phi = 0°$ (Fig. 13). The LCE with $\theta_0 = 90°$ shows little director rotation ahead of the crack tip due to the parallel loading. Conversely, in the LCE with $\theta_0 = 60°$, the director rotation decreases monotonically with the distance ρ/a. However, in the LCEs with $\theta_0 = 30°$ and 45°, the director rotation non-monotonically decreases and then increases with ρ/a. This peculiar observation can be attributed to the inhomogeneous principal stress distribution at the crack tip and the remote region, which is significantly influenced by the initial director. Close to the crack tip, the director aligns tangentially to the crack opening surface resulting in a substantial director reorientation. Consequently, the observed decrease in the director rotation with increasing ρ/a is ascribed to the reduction of stress concentration, and as a result, the director deviates from the tangent direction of the crack surface. As one moves farther away from the crack tip, the director rotation increases again primarily because the director undergoes considerable reorientation to align itself with the remote stretching direction ~90°.

4.2 Displacement measurement via digital image correlation (DIC)

The displacement distribution in the edge-cracked LCE samples subjected to external loading was measured using DIC. Fig. 14(a) and 14(b) illustrate the normalized displacement u_2/L along X_2 with respect to the bottom boundary of the specimen near the crack tip for the LCE with $\theta_0 =$

90° at $\varepsilon^{\infty} = 10\%$. Both experimental and FEM simulation results show a symmetrical deformation about $\phi = 0°$, which is consistent with the symmetrical rotation of the director, and in line with the symmetrical deformation of neo-Hookean materials (Knowles and Sternberg, 1973). Not surprisingly, near the crack tip, the maximum deformation, $u_2/L \approx 0.1$, occurs behind the crack tip in the LCE with $\theta_0 = 90°$ due to rigid-body motion on the free surface, while at the crack tip, the displacement is $u_2/L = 0.05$. However, when the initial director is tilted away from the remote strain, u_2/L is no longer symmetrical (Fig. 14(c-h)). This asymmetric deformation pattern has been indicated in the preceding section to be caused by the asymmetric director rotation, and consequently the asymmetric spontaneous strain, including the shear components. As θ_0 decreases, the displacement u_2 near the crack becomes smaller due to the bulk director rotation, but meanwhile the location of the maximum displacement shifts to the top-right corner due to severe shear deformation under the confinement of a clamped boundary condition. Fig. 15 exhibits the displacement u_1/a and u_2/a ahead of the crack tip from DIC and FEM. Upon comparing the DIC and FEM results (Fig. 14 and Fig. 15), it is evident that the displacement contours from the simulations closely resemble the experimental findings, thereby validating the theoretical modeling approach.

The crack tip opening displacement is dramatically influenced by the rotation of the director (Fig. 16). To compare the crack-tip opening displacement, we calculate the difference in movement between the top and the bottom crack surfaces, $\delta u_2 = u_2^{top} - u_2^{bot}$ for LCEs with different θ_0. For the LCE with $\theta_0 = 90°$, the director rotation mainly occurs near the crack ($\phi \neq 0°$, $\rho \to 0$). The spontaneous strain induced by director rotation leads to additional compressive strain normal to the crack surface, so the crack tends to open more than that of a neo-Hookean material. Conversely, for the LCEs with $\theta_0 = 60°$, 45° and 30°, the crack opening is notably smaller than that exhibited by a neo-Hookean material. There are two reasons for the reduced crack opening in LCEs with tilted initial directors. First, the overall director rotation leads to bulk softening. Second, the local director rotation at the crack tip, inducing opposite shear strain around the domain wall, leads to sharp changes on the crack surface and asymmetrical crack opening pattern; see Fig. 10, where a sharp turning occurs, constraining the extent of the opening. Meanwhile, the director rotation direction is reversed in comparison to the case of $\theta_0 = 90°$, and consequently, the associated spontaneous strain constrains the opening. This phenomenon can be proved by examining the deformed FEM elements near the crack tip (Fig. 17). It becomes evident that the elements in the case of $\theta_0 = 90°$ distort greater than that of a neo-Hookean material, indicating that the associated spontaneous strain facilitates the deformation, while in the case of $\theta_0 = 30°$, the elements display reduced distortion at the same small applied strain ($\varepsilon^{\infty} = 2\%$), suggesting that the different directions of director rotation from those of $\theta_0 = 90°$ impose spontaneous strain that limits deformation. As the director near the crack tip rotates mainly following the deformation at $\varepsilon^{\infty} > 2\%$, the bulk softening starts to dominate the crack opening, resulting in a smaller crack opening for a smaller initial director θ_0. The corresponding deformation of the

FEM elements at $\varepsilon^{\infty} = 4\%$ (Supplementary Fig. S6) also reveals that in the case of $\theta_0 = 30°$, the elements exhibit significantly less deformation than that of the neo-Hookean material and LCE with $\theta_0 = 90°$ due to the combined contribution of bulk softening and local director rotation.

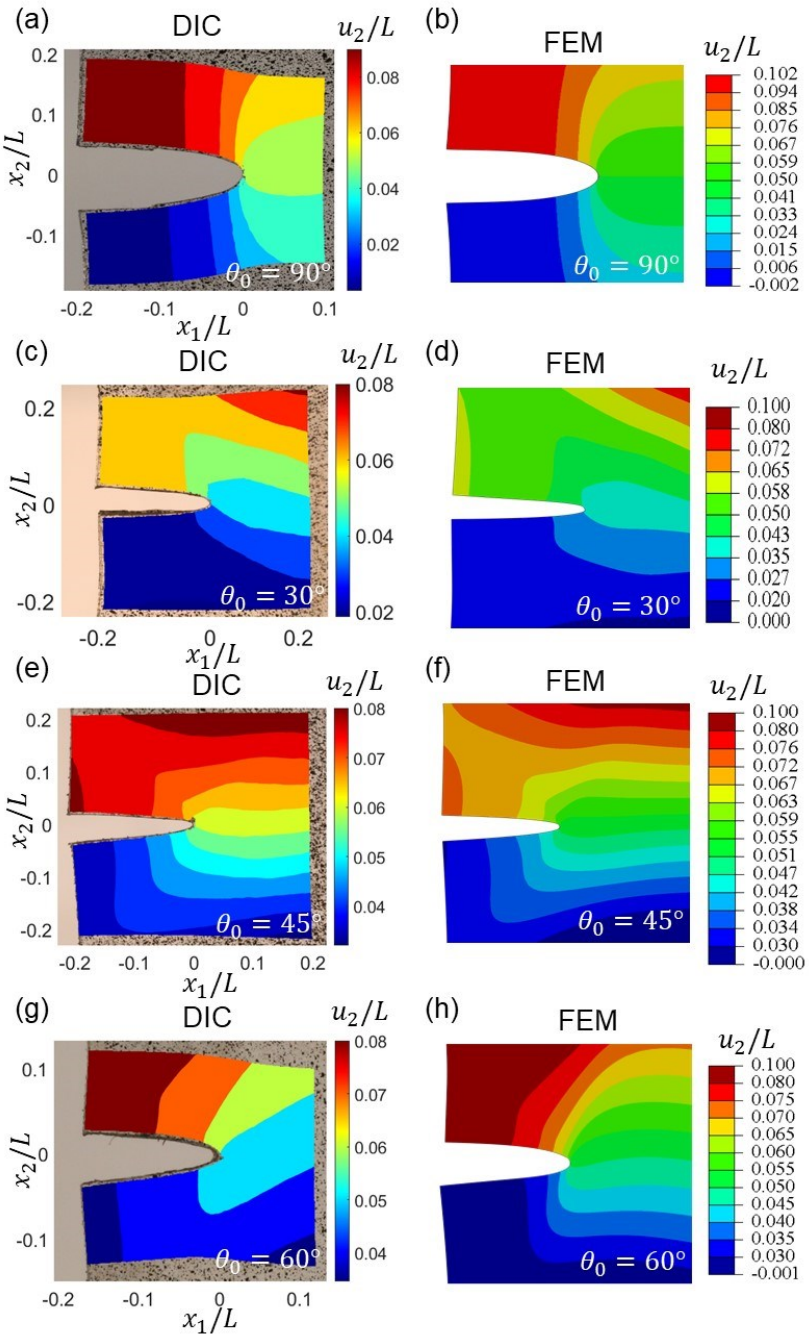

Fig. 14 Comparing the displacement fields from DIC and FEM. The distribution of the normalized displacement u_2/L around the crack of the LCEs with (a, b) $\theta_0 = 90°$, (c, d) 30°, (e, f) 45° and (g, h) 60° at $\varepsilon^{\infty} = 10\%$ from (a, c, e, g) DIC and (b, d, f, h) FEM.

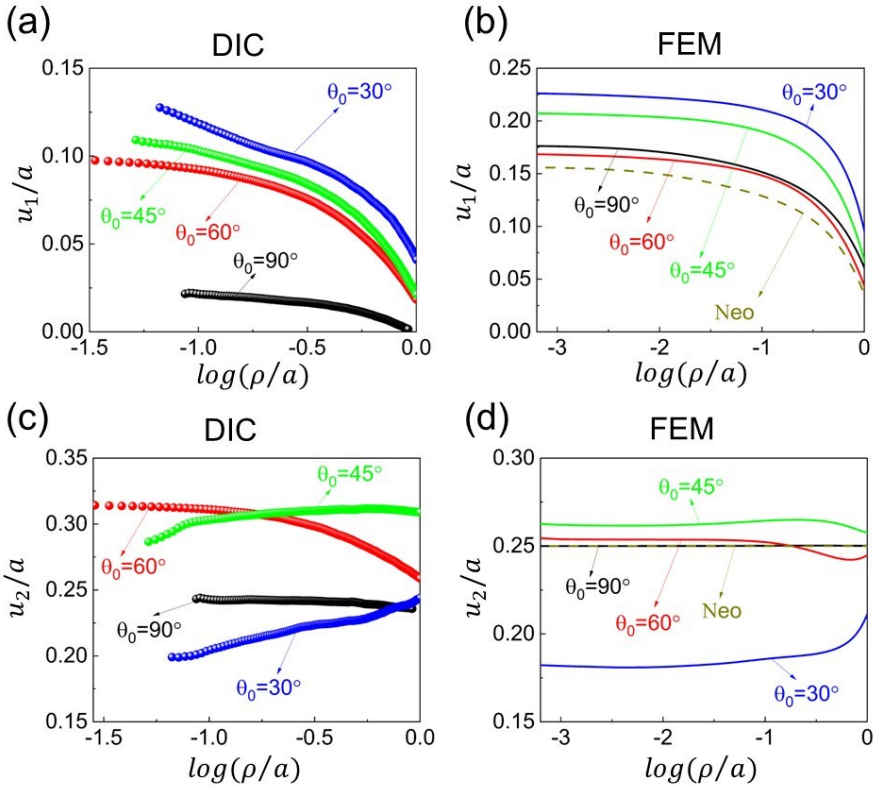

Fig. 15 Displacement distributions ahead of the crack tip at $\varepsilon^{\infty} = 10\%$. Normalized displacement (a, b) u_1/a and (c, d) u_2/a ahead of the crack tip for LCEs with $\theta_0 = 90°, 60°, 45°, 30°$ obtained from (a, c) DIC and (b, d) FEM. The simulation and experiment results show a consistent trend for LCEs with different initial directors.

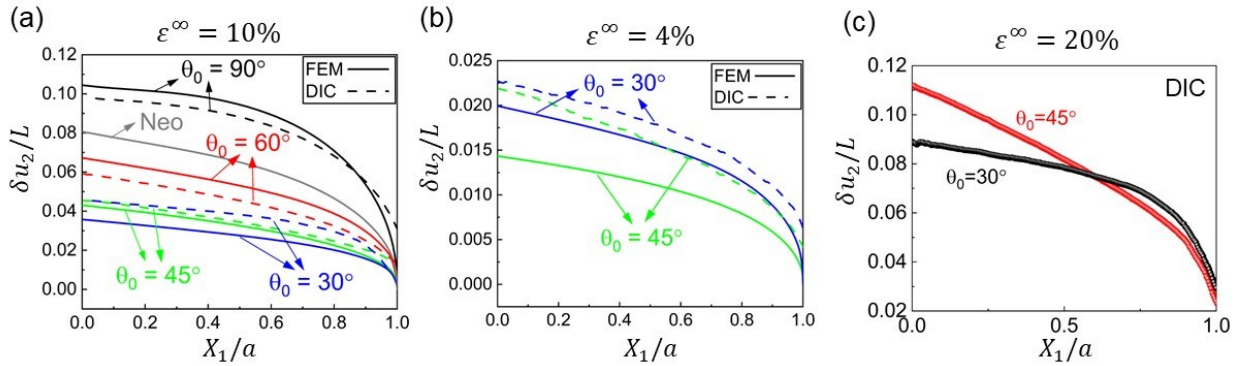

Fig. 16 Crack opening displacement. Normalized crack tip opening displacement $\delta u_2/L$ from the DIC (dashed lines) and FEM (solid lines) for the LCEs with different θ_0 at (a) $\varepsilon^{\infty} = 10\%$ and

(b) 4%. (c) Normalized crack tip opening displacement $\delta u_2/L$ measured from DIC for the LCEs with $\theta_0 = 30°$ and $45°$ at $\varepsilon^\infty = 20\%$.

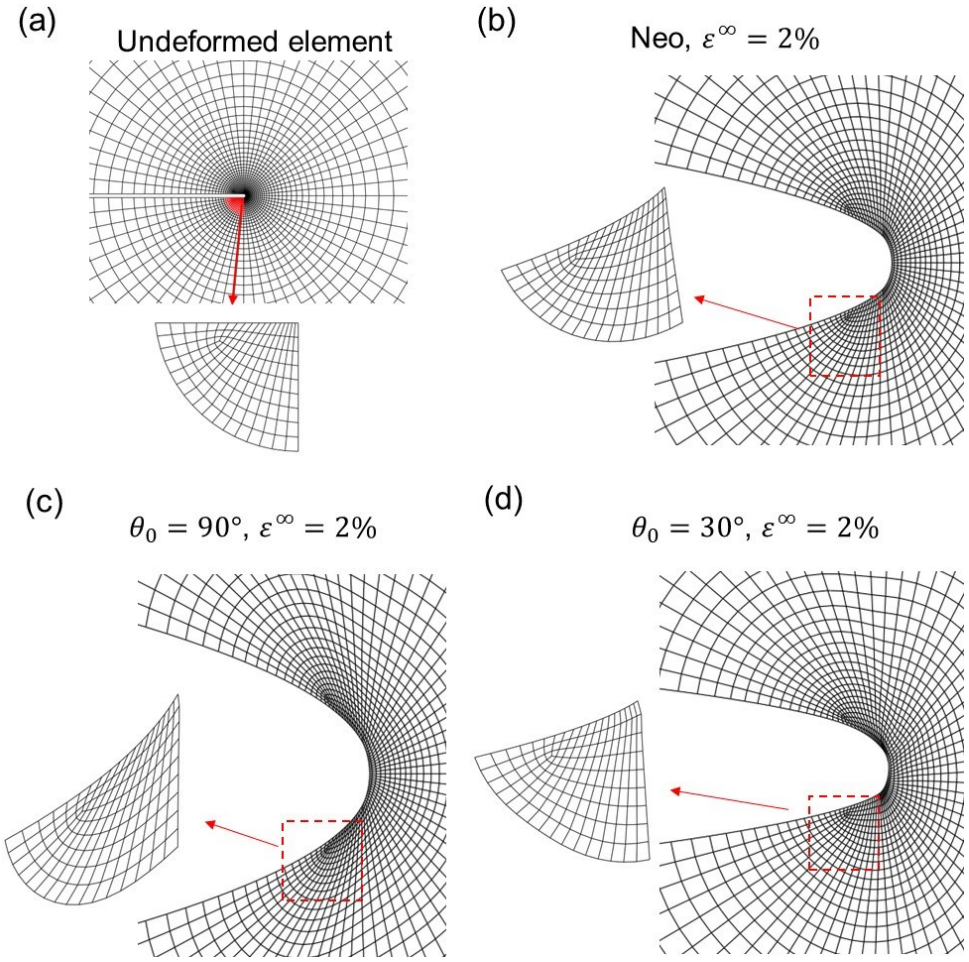

Fig. 17 Comparing the deformation of the FEM elements around the crack tip for LCEs and neo-Hookean materials at $\varepsilon^\infty = 2\%$. (a) Undeformed elements. Crack opening and element deformation at $\varepsilon^\infty = 2\%$ for (b) a neo-Hookean material and a LCE with (c) $\theta_0 = 90°$ and (d) $\theta_0 = 30°$.

It is evident that the crack opening displacement measured for the LCE with $\theta_0 = 30°$ is smaller than that of $\theta_0 = 45°$ at a high remote strain $\varepsilon^\infty = 20\%$ (Fig. 16(c) and Supplementary Fig. S7), but interestingly, it is larger than that of $\theta_0 = 45°$ at a relatively low remote strain $\varepsilon^\infty = 10\%$ and 4% (Fig. 16(b)). The simulation results present the same trend as the experiment, although in the simulations the crack opening displacement for the LCE with $\theta_0 = 45°$ surpasses that of $\theta_0 = 30°$ at a smaller strain between 4% and 10%. Drawing upon the findings by Peng et al. (Peng et al., 2023) that LCEs with $\theta_0 = 45°$ exhibits the minimized stress concentration fac-

tor, we postulate that at a small strain the magnitude of the crack opening is predominantly influenced by the director near the crack tip, and consequently, the director rotation in the LCE with $\theta_0 = 45°$ reduces its crack opening more compared to LCEs with other initial directors. As the remote strain increases, the bulk softening plays a more dominant role in affecting the crack opening, and therefore, the LCE with $\theta_0 = 30°$, which has a stronger bulk softening due to director rotation, has a smaller crack opening than that of $\theta_0 = 45°$. The competition of the two factors leads to the positive-to-negative transition of the difference in the crack opening between the LCEs with $\theta_0 = 30°$ and $\theta_0 = 45°$ as the remote strain increases.

5 Evaluation of fracture behavior

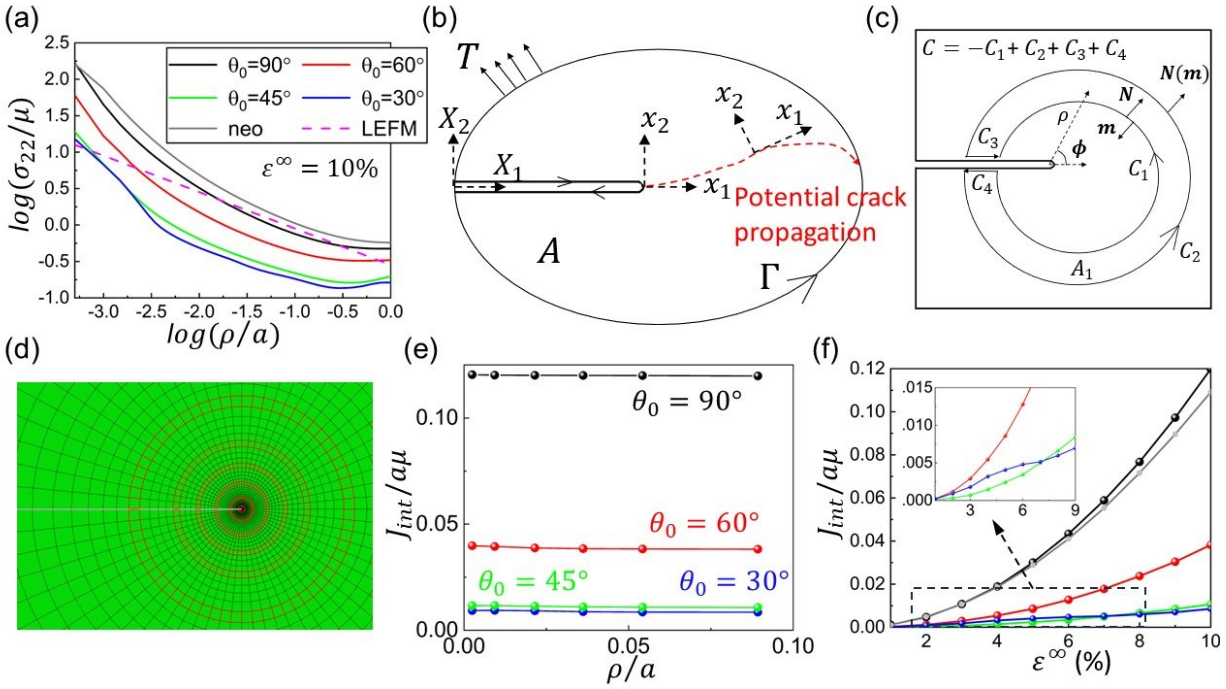

Fig. 18 Stress distribution ahead of crack tips and J-integral. (a) Normalized Cauchy stress distribution ahead of the crack tips for the LCEs of $\theta_0 = 30°, 45°, 60°$ and $90°$, a neo-Hookean material, and a linearly elastic material at $\varepsilon^\infty = 10\%$. (b) Schematics of a contour to evaluate the J integral and potential crack trajectory in the reference configuration. (c) Region A_1 enclosed by the contour $C = -C_1 + C_2 + C_3 + C_4$ and (d) five different integral paths around the crack tip are highlighted in the FEM model to calculate the J-integral. (e) Normalized J-integral based on six paths of different ρ/a, verifying its path-independency for LCEs. (f) Normalized J_{int} as a function of the remote strain ε^∞ for the LCEs with $\theta_0 = 30°, 45°, 60°$ and $90°$, and a neo-Hookean material. (f) shares the same legend as (a).

To evaluate the fracture behavior, we analyze the stress ahead of the crack tip and the energy release rate for LCEs with different initial directors. We plot the Cauchy stress σ_{22} as a function of the distance from the crack tip, ρ/a, at $\varepsilon^\infty = 10\%$ in Fig. 18(a), and compare with that of a

neo-Hookean material and a linearly elastic material (Broberg, 1999). In general, LCEs present a similar stress distribution to that of a neo-Hookean material. The LCE with $\theta_0 = 90°$ displays slightly lower stress values compared to the neo-Hookean case. We postulate that this discrepancy arises from the stress redistribution caused by the reorientation of the director in the LCE. Specifically, the director along $\phi = 0°$ undergoes limited rotation, while more director rotation occurs at $\phi > 0°$ and $\phi < 0°$. Consequently, the material along $\phi = 0°$ behaves stiffer than the surrounding regions, leading to stress redistribution, and resulting in lower stress values compared to those of a neo-Hookean material. For LCEs with tilted initial directors, significant director rotation occurs, inducing large spontaneous strain, resulting in considerably lower stress values. It is important to note that when the initial director is tilted relative to the applied strain, the maximum stress may not be located at $\phi = 0°$ as described in the previous sections. Therefore, the crack propagation may not follow the direction of $\phi = 0°$. To gain a deeper understanding of the fracture behavior, further investigations are required to observe and analyze the crack propagation.

Under the plane strain condition, we further calculate the energy release rate in a two-dimensional LCE. Consider a 2D deformed LCE body, as shown in Fig. 18(b). We eliminate the dissipation energy while calculating the energy release rate due to extremely small values of viscosity. In the absence of the body force, the energy release rate G is defined as the change in the total potential energy per area of the crack growth:

$$G = -\frac{dU}{da} = -\int_A \frac{df_r}{da} dA + \int_\Gamma T_i \frac{du_i}{da} dS, \quad (11)$$

where U is the total potential energy defined as $U = \int_A f_r dA - \int_\Gamma \boldsymbol{T} \cdot \boldsymbol{u} dS$, with $f_r(\boldsymbol{F}, \boldsymbol{d}, \nabla \boldsymbol{d})$ the elastic energy density of a LCE, $\boldsymbol{T}$ the prescribed surface traction on the boundary Γ in the reference configuration, and A the total area of the body in the reference configuration. Introduce a coordinate system $x_i = X_i - a\delta_{i1}$ (i =1, 2), where the origin of $\boldsymbol{x}$ locates at the crack tip in the current configuration Fig. 18(b). Although for a LCE with a tilted director, the crack trajectory may not conform to the horizontal direction, we assume it is smooth, so at the onset of propagation, the crack direction still aligns with the $x_1 -$ axis (Lu et al., 2021). Based on the chain rule, we get

$$\frac{d}{da} = \frac{\partial}{\partial a} + \frac{\partial x_1}{\partial a}\frac{\partial}{\partial x_1} = \frac{\partial}{\partial a} - \frac{\partial}{\partial x_1} = \frac{\partial}{\partial a} - \frac{\partial}{\partial X_1}. \quad (12)$$

Substituting Eq. (12) into Eq. (11) we can calculate G as

$$G = -\int_A \left(\frac{\partial f_r}{\partial \boldsymbol{F}}\frac{\partial \boldsymbol{F}}{\partial a} + \frac{\partial f_r}{\partial \boldsymbol{d}}\frac{\partial \boldsymbol{d}}{\partial a} + \frac{\partial f_r}{\partial \nabla \boldsymbol{d}}\frac{\partial \nabla \boldsymbol{d}}{\partial a} - \frac{\partial f_r}{\partial X_1}\right) dA + \int_\Gamma T_i \left(\frac{\partial u_i}{\partial a} - \frac{\partial u_i}{\partial X_1}\right) dS. \quad (13)$$

Then applying the divergence theorem, we can rewrite Eq. (13) to

$$G = -\int_A \left(\frac{\partial f_r}{\partial \boldsymbol{F}}\frac{\partial \boldsymbol{F}}{\partial a} + \frac{\partial f_r}{\partial \boldsymbol{d}}\frac{\partial \boldsymbol{d}}{\partial a} - div_X\left(\frac{\partial f_r}{\partial \nabla \boldsymbol{d}}\boldsymbol{F}^{-\boldsymbol{T}}\right)\frac{\partial \boldsymbol{d}}{\partial a} - \frac{\partial f_r}{\partial X_1}\right)dA \\ - \int_\Gamma \left(\frac{\partial f_r}{\partial \nabla \boldsymbol{d}}\boldsymbol{F}^{-\boldsymbol{T}}\right)\boldsymbol{N}\frac{\partial \boldsymbol{d}}{\partial a}dS + \int_\Gamma T_i\left(\frac{\partial u_i}{\partial a} - \frac{\partial u_i}{\partial X_1}\right)dS. \quad (14)$$

As $\nabla \boldsymbol{d}$ only exists in the Frank energy, which is considerably small compared to the total elastic energy (Jiang et al., 2021; Warner and Terentjev, 2007). To simplify the calculation, we eliminate the term associated with $\nabla \boldsymbol{d}$ when evaluating the energy release rate. Using the governing equations (6) and (7), we can rewrite Eq. (14) as the following Eq. (15), which recovers the classical form of the J-integral, although now $\boldsymbol{d}$ is a new independent variable in the free energy density of LCEs

$$G = J_{int} = \int_\Gamma \left(f_r N_1 - S_{iJ}N_J\frac{\partial u_i}{\partial X_1}\right)dS, \quad (15)$$

where $\boldsymbol{N}$ is the outward normal to the path Γ in the reference configuration and $\boldsymbol{S} = \partial f_r/\partial \mathbf{F}$ is the first Piola–Kirchhoff stress. Eq. (15) not only holds true for the boundary of the body in the path integration, but also remains valid for any arbitrary path from the bottom crack surface to the top crack surface (Kanninen et al., 1986; Rice, 1968), so Γ can be denoted as an arbitrary path.

In FEM, it is more convenient to conduct an area integration than a line integration, so we convert Eq. (15) to an area integration (Li et al., 1985). Now consider a closed curve denoted by $C = -C_1 + C_2 + C_3 + C_4$ that bounds an area A_1 with a outward normal vector $\boldsymbol{m}$ (Fig. 18(c)). Based on the divergent theorem, the line integration of the J-integral, Eq. (15), over the contour C can be rewritten as

$$J_{int} = \int_{A_1}\left(-f_r\frac{\partial q}{\partial X_1} + S_{iJ}\frac{\partial u_i}{\partial X_1}\frac{\partial q}{\partial X_J}\right)dA, \quad (16)$$

where q is a sufficiently smooth function varying from unity on C_1 to zero on C_2; $\boldsymbol{m}$ is the outward unit vector normal to C. Therefore, $\boldsymbol{m} = -\boldsymbol{N}$ on C_1 and $\boldsymbol{m} = \boldsymbol{N}$ on C_2. The integrals along C_3 and C_4 are zero as no surface traction on the crack surface and $m_1 = 0$. Therefore, Eq (16) and Eq. (15) are equivalent. Applying the divergence theorem, we get an area integral J_{int}

$$J_{int} = \int_{A_1}\left(-f_r\frac{\partial q}{\partial X_1} + S_{iJ}\frac{\partial u_i}{\partial X_1}\frac{\partial q}{\partial X_J}\right)dA. \quad (17)$$

The path-independency of the J-integral is presented in Fig. 18(e), where the domain integral is computed at $\varepsilon^\infty = 10\%$ for various contours C_1 of different distances ρ/a (Fig. 18d)). We calculate the J-integral for LCEs with different initial directors (Fig. 18(f)). Generally, a smaller θ_0 leads to a lower J_{int}. However, the LCE with $\theta_0 = 30°$ shows higher J_{int} than that of $\theta_0 = 45°$ at a small remote strain $\varepsilon^\infty < \sim 7\%$; conversely, it shows a lower J_{int} at a large remote strain $\varepsilon^\infty > \sim 7\%$, similar to the trend of the crack opening displacement. We propose that a combined

effect of bulk softening in the remote region and the director rotation near the crack tip influences both the J-integral value and crack displacement opening. Specifically, at a small remote strain, the energy release rate is dominated by the substantial director rotation occurring around the crack tip; conversely, at a high remote strain, the energy release rate is dominated by the overall director rotation. Compared to the behavior of neo-Hookean materials, LCEs under parallel loading present slightly higher J_{int}, while LCEs with tilted stretching consistently show significantly smaller J_{int}. The deviation of J_{int} of LCEs from that of neo-Hookean materials is primarily attributed to the inhomogeneous stress redistribution caused by the director rotation to the direction of the local principle stress around the crack tip and in the remote region. As previously demonstrated (Supplementary Fig. S1), LCEs exhibit softer behavior as the initial director deviates more from the loading direction. As a result, the stress distribution becomes intricate, as LCEs exhibit different levels of softening around the crack tip due to varying director reorientation. This phenomenon gives rise to highly inhomogeneous stress, strain and director in the vicinity of a crack tip, leading to higher ($\theta_0 = 90°$) or lower ($\theta_0 = 30°, 45°$ and $\theta_0 = 60°$) J_{int} than that of neo-Hookean materials.

6 Conclusion

In this work, we combine simulations and experiments to provide a comprehensive investigation of the unique crack-tip fields of LCEs with various initial directors induced by their stress-director coupling behavior. We limit ourselves to obvious crack blunting but without crack propagation in this study. From FEM simulations, we predict inhomogeneous and significant director reorientation of LCEs, which leads to unique stress and strain distributions in contrast to those in traditional neo-Hookean materials; in experiments, we successfully measure the displacement field by the DIC and the inhomogeneous director reorientation by the optical polariscopic method, validating the findings in the FEM simulations. Based on the consistent results from the FEM and experiments, we reveal the unexpected occurrence of opposite director rotation near the crack tip of LCEs, and dramatically different energy release rates and crack opening displacements of LCEs from traditional elastomers.

Since the unique mechanical responses of a LCE are mainly governed by its director rotation, we demonstrate that the initial director can significantly influence its crack-tip fields and fracture behavior. For an edge-cracked LCE subjected to stretching parallel to its director, the director near the crack tip rotates clockwise at the polar angle $\phi < 0°$ and counter-clockwise at $\phi > 0°$, inducing a spontaneous strain field symmetric about the crack, and resulting in smooth and elliptical-shaped stress/strain contour lines. In contrast, for an edge-cracked LCE with a tilted initial director with respect to the loading, the director undergoes rotation throughout the bulk sample, while exhibiting more substantial rotation near the crack tip. A domain wall is observed along a critical polar angle; the director rotates clockwise in the region with a larger polar angle and counter-clockwise in the region with a smaller polar angle. The director rotates significantly in

the vicinity of the domain wall, resulting in elliptical stress/strain contour lines with the smoothest gradient direction close to the critical polar angle, and consequently, the stress/strain is no longer symmetrical about the crack. As the tilted angle θ_0 increases, the critical polar angle of the domain wall increases, and the crack opening decreases. Compared to a neo-Hookean material, a LCE with a director parallel to stretching, $\theta_0 = 90°$, exhibits a higher energy release rate and larger crack opening, while a LCE with a tilted director presents a much lower energy release rate and smaller crack opening primarily caused by bulk softening induced by overall director rotation. Interestingly, director rotation around the crack tip can be non-monotonic, because at a small strain the director undergoes rapid rotation and tends to align to the local principal stress direction; after the director aligns with the principal stress direction, the director rotates gradually following the macroscopic deformation as the strain further increases.

This work provides a valuable understanding on the director, stress and strain distributions in the vicinity of a crack tip of LCEs, which offers insights into designing LCEs with enhanced fracture properties for long-time applications. The findings and methodology presented in this work lay a solid foundation for further investigation of fracture behavior in LCEs, taking into account their viscoelasticity and crack propagation. Although in this work we load LCEs slowly enough to reach quasi-equilibrium states, LCEs are highly viscoelastic (Clarke and Terentjev, 1999; Hotta and Terentjev, 2001; Warner and Terentjev, 2007), involving multiple relaxation time scales of network relaxation and director rotation. It will be intriguing to investigate the rate-dependent crack-tip fields and fracture behavior for LCEs with different initial directors. Furthermore, based on the stress/strain contour lines obtained from this work, it is conceivable to predict that the crack propagation paths in LCEs with different θ_0 can be quite different. Specifically, it is expected that a tilted crack path occurs when the initial director is tilted from the loading direction. All those will be our future work.

Acknowledgments

This work is supported by the National Science Foundation (NSF) through Grant No. CMMI-1925790. B.H. is supported by a NSF Research Experiences for Undergraduates (REU) supplement through Grant No. CMMI-2227512. The authors acknowledge the insightful discussions with Prof Yongzhong Huo at Fudan University.

Appendix

A.1 Viscoelastic constitutive model

To simulate the crack-tip fields of LCEs, we implement the constitutive model into a FEM code. Though we assume the LCE samples are loaded slowly enough to reach quasi-equilibrium so that we do not need to consider their viscoelasticity, a small dissipation is added to the model to avoid convergence issues during analyses. Following Zhang et al. (Zhang et al., 2019), we use

a simple Rayleigh dissipation density function to represent the viscosity of the network and the director

$$R = R\left(\dot{\boldsymbol{\varepsilon}}, \widetilde{\boldsymbol{d}}\right) = \frac{1}{2}\eta_d \widetilde{\boldsymbol{d}}^2 + \frac{1}{2}\eta_0 tr(\dot{\boldsymbol{\varepsilon}}^2), \tag{A1}$$

where $\dot{\boldsymbol{\varepsilon}}$ is the strain rate tensor $\dot{\boldsymbol{\varepsilon}} = \dot{\boldsymbol{F}}\boldsymbol{F}^{-1}$, $\widetilde{\boldsymbol{d}}$ is the corotational time derivative $\widetilde{\boldsymbol{d}} = \dot{\boldsymbol{d}} - \boldsymbol{W}\boldsymbol{d}$ with $\boldsymbol{W}$ the spin tensor $\boldsymbol{W} = (\nabla\dot{\boldsymbol{u}} - \nabla\dot{\boldsymbol{u}}^T)/2$, and η_0 and η_d are the viscosity of the network extension and director rotation, respectively, which are assumed very small, $\eta_0/\mu = \eta_d/\mu = 10^{-4}s$. In our simulations, we applied a low loading rate to ensure the quasistatic condition. The energy balance can be expressed as

$$\dot{W} - \int_{\Omega_0} \dot{f}_r dV = \int_{\Omega_0} \left(\frac{\partial R}{\partial \widetilde{\boldsymbol{d}}} : \widetilde{\boldsymbol{d}} + \frac{\partial R}{\partial \dot{\boldsymbol{\varepsilon}}} : \dot{\boldsymbol{\varepsilon}}\right) dV, \tag{A2}$$

where $\dot{W}$ is the external power and f_r is the free energy density, as elaborated in the main text.

Due to the addition of the Rayleigh dissipation, we could re-derive the governing equations associated with $\dot{\boldsymbol{u}}$ and $\dot{\boldsymbol{d}}$ as the following, which are slightly different from Eqs. (6)-(8)

$$div(\boldsymbol{\sigma}) + \boldsymbol{b} = \boldsymbol{0}, \tag{A3}$$

$$\eta_d \dot{\boldsymbol{d}} \times \boldsymbol{d} = \eta_d \boldsymbol{W}\boldsymbol{d} \times \boldsymbol{d} - \mu\left(\left(l_{\parallel}^{-1} - l_{\perp}^{-1}\right)\boldsymbol{F}\boldsymbol{l_0}\boldsymbol{F}^T\boldsymbol{d} + \alpha\boldsymbol{F}(\boldsymbol{I} - \boldsymbol{d_0} \otimes \boldsymbol{d_0})\boldsymbol{F}^T\boldsymbol{d}\right) \times \boldsymbol{d} + K\nabla^2\boldsymbol{d} \times \boldsymbol{d}, \tag{A4}$$

where the Cauchy stress $\boldsymbol{\sigma}$ is

$$\boldsymbol{\sigma} = J^{-1}\mu(\boldsymbol{l}^{-1}\boldsymbol{F}\boldsymbol{l_0}\boldsymbol{F}^T + \alpha\boldsymbol{d} \otimes (\boldsymbol{I} - \boldsymbol{d_0} \otimes \boldsymbol{d_0})\boldsymbol{F}^T\boldsymbol{d} \cdot \boldsymbol{F}^T - \boldsymbol{I}) + 2B(J-1)\boldsymbol{I} - J^{-1}K(\nabla\boldsymbol{d})^T\nabla\boldsymbol{d} + J^{-1}\eta_0\dot{\boldsymbol{\varepsilon}} + \frac{J^{-1}}{2}\eta_d(\boldsymbol{d} \otimes \left(\dot{\boldsymbol{d}} - \boldsymbol{W}\boldsymbol{d}\right) - (\dot{\boldsymbol{d}} - \boldsymbol{W}\boldsymbol{d}) \otimes \boldsymbol{d}). \tag{A5}$$

If the viscosity is not considered, Eqs. (A4)(A5) recover Eqs. (7)(8) by eliminating the terms involving η_0 and η_d. The first two terms in Eq. (A5) can be rewritten as the following so that the first term is independent of the director, which is more convenient for the implementation of the UEL later

$$\boldsymbol{\sigma} = J^{-1}\mu\left(l_{\perp}^{-1}\boldsymbol{F}\boldsymbol{l_0}\boldsymbol{F}^T + \left(l_{\parallel}^{-1} - l_{\perp}^{-1}\right)\boldsymbol{d} \otimes \boldsymbol{F}\widehat{\boldsymbol{l_0}}\boldsymbol{F}^T\boldsymbol{d} - \boldsymbol{I}\right) + 2B(J-1)\boldsymbol{I} - J^{-1}K(\nabla\boldsymbol{d})^T\nabla\boldsymbol{d} + J^{-1}\eta_0\dot{\boldsymbol{\varepsilon}} + \frac{J^{-1}}{2}\eta_d(\boldsymbol{d} \otimes \left(\dot{\boldsymbol{d}} - \boldsymbol{W}\boldsymbol{d}\right) - (\dot{\boldsymbol{d}} - \boldsymbol{W}\boldsymbol{d}) \otimes \boldsymbol{d}), \tag{A6}$$

with $\widehat{\boldsymbol{l_0}} = \boldsymbol{l_0} + \alpha(\boldsymbol{I} - \boldsymbol{d_0} \otimes \boldsymbol{d_0})/\left(l_{\parallel}^{-1} - l_{\perp}^{-1}\right)$. Under the plane strain condition, the director degenerates to $\boldsymbol{d} = (\cos(\theta), \sin(\theta), 0)$, where θ is utilized as the variable to represent the angle between the director and the $X_1 -$ axis. Thereby, the governing equation Eq. (A4) can be further simplified as

$$\eta_d\dot{\theta} + \eta_d W_{12} - \sigma^d{}_{21} + \sigma^d{}_{12} - K\nabla^2\theta = 0, \tag{A7}$$

with $\boldsymbol{\sigma^d} = \mu(l_{\parallel}^{-1} - l_{\perp}^{-1})\boldsymbol{d} \otimes \boldsymbol{F}\widehat{\boldsymbol{l_0}}\boldsymbol{F}^T\boldsymbol{d}$. The boundary conditions associated with the displacement and the director field are

$$\boldsymbol{\sigma} \cdot \boldsymbol{n} = \boldsymbol{t}, \tag{A8}$$

$$J^{-1}K\boldsymbol{\nabla d} \cdot \boldsymbol{n} = \boldsymbol{0}, \tag{A9}$$

where $\boldsymbol{t}$ is the traction in the current configuration on the surface, and $\boldsymbol{n}$ represents the unit outer vector normal to the deformed surface boundary. In this study, we assume no body force and surface traction.

A.2 Numerical solution procedure

Based on the FEM, the two coupled Eqs. (A3) (A4) are solved via a Newton procedure by gradually vanishing the corresponding residuals on the element level. We use a method similar to Chester et al.(Chester et al., 2015) to implement the coupled equations into a user element subroutine, UEL, in the commercial finite element software, ABAQUS. The trial solutions for the displacement and the director angle are interpolated inside each element by:

$$\boldsymbol{u} = \sum \boldsymbol{u^A} N^A, \tag{A10}$$

$$\theta = \sum \theta^A N^A, \tag{A11}$$

where A={1,2,3 …} denotes the nodes of a given element, $\boldsymbol{u^A}$ and θ^A represent the values of the displacement and the director angle at node A, and N^A represents the corresponding shape function. In the absence of body forces, we employ a standard Galerkin approach with two weight functions $\boldsymbol{w_1} = \sum \boldsymbol{w_1}^{\boldsymbol{A}} N^A$ and $w_2 = \sum {w_2}^A N^A$, where $\boldsymbol{w_1}$ and w_2 have the same shape function as the trial solutions and vanish under the Dirichlet boundary condition. In the absence of body forces, we can get two weak forms for Eqs. (A3) (A4)

$$\int_{\Omega_c} \boldsymbol{w_1} \cdot div(\boldsymbol{\sigma}) dv = 0, \tag{A12}$$

$$\int_{\Omega_c} w_2\left(\eta_d \dot{\theta} + \eta_d W_{12} - {\sigma^d}_{21} + {\sigma^d}_{12} - K\nabla^2\theta\right) dv = 0\,. \tag{A13}$$

Through the divergence theorem and boundary conditions in Eqs. (A8) (A9), we can get the following element-level equations

$$\int_{\Omega_c} \frac{\partial N^A}{\partial x} \boldsymbol{\sigma} dv = \int_{\Gamma_c} N^A \boldsymbol{t} da, \tag{A14}$$

$$\int_{\Omega_c} N^A\left(\eta_d \dot{\theta} + \eta_d W_{12} - {\sigma^d}_{21} + {\sigma^d}_{12}\right) dv = -\int_{\Omega_c} K \frac{\partial N^A}{\partial x} \nabla\theta dv. \tag{A15}$$

We solve the coupled equations through the Newton's method by defining two residuals $\boldsymbol{R_u^A}$ and R_θ^A for the displacement and the director

$$\boldsymbol{R_u^A} = -\int_{\Omega_c} \frac{\partial N^A}{\partial x}\boldsymbol{\sigma} dv + \int_{\Gamma_c} N^A \boldsymbol{t} da, \tag{A16}$$

$$R_\theta^A = -\int_{\Omega_c} (N^A\left(\eta_d \dot{\theta} + \eta_d W_{12} - {\sigma^d}_{21} + {\sigma^d}_{12}\right) + K\frac{\partial N^A}{\partial x}\nabla\theta) dv. \tag{A17}$$

In addition to the residuals, ABAQUS/Standard requires the matrix AMATRX to be evaluated and updated for the iterative Newton solver. AMATRX is defined as an array containing the contribution of this element to the Jacobian (stiffness) or other matrix of the overall system of equations, which is given by:

$$K = \begin{bmatrix} K_{u_1u_1}^{11} & K_{u_1u_2}^{11} & K_{u_1\theta}^{11} & & K_{u_1u_1}^{14} & K_{u_1u_2}^{14} & K_{u_1\theta}^{14} \\ K_{u_2u_1}^{11} & K_{u_2u_2}^{11} & K_{u_2\theta}^{11} & \cdots & K_{u_2u_1}^{14} & K_{u_2u_2}^{14} & K_{u_2\theta}^{14} \\ K_{\theta u_1}^{11} & K_{\theta u_2}^{11} & K_{\theta\theta}^{11} & & K_{\theta u_1}^{14} & K_{\theta u_2}^{14} & K_{\theta\theta}^{14} \\ & \vdots & & \ddots & & \vdots & \\ K_{u_1u_1}^{41} & K_{u_1u_2}^{41} & K_{u_1\theta}^{41} & & K_{u_1u_1}^{44} & K_{u_1u_2}^{44} & K_{u_1\theta}^{44} \\ K_{u_2u_1}^{41} & K_{u_2u_2}^{41} & K_{u_2\theta}^{41} & \cdots & K_{u_2u_1}^{44} & K_{u_2u_2}^{44} & K_{u_2\theta}^{44} \\ K_{\theta u_1}^{41} & K_{\theta u_2}^{41} & K_{\theta\theta}^{41} & & K_{\theta u_1}^{44} & K_{\theta u_2}^{44} & K_{\theta\theta}^{44} \end{bmatrix}, \tag{A18}$$

where the Jacobian stiffness $K_{u_iu_k}^{AB} = -\partial R_{u_i}^A/\partial u_k^B$, $K_{u_i\theta}^{AB} = -\partial R_{u_i}^A/\partial\theta^B$, $K_{\theta\theta}^{AB} = -\partial R_\theta^A/\partial\theta^B$, and $K_{\theta u_i}^{AB} = -\partial R_\theta^A/\partial u_i^B$ with B={1,2,3 …} denoting the nodes of the element, and u_1 and u_2 denote the displacements in the X_1 and X_2 directions, respectively. In this study, we utilize a 2D plane-strain 4-node linear quadrilateral elements, and hence AMATRX is a 12 by 12 matrix.

Here we rewrite each Jacobian stiffness in the index notation

$$K_{u_iu_k}^{AB} = \frac{-\partial R_{u_i}^A}{\partial u_k^B} = \frac{\partial\left(\int_{\Omega_c}\frac{\partial N^A}{\partial x_j}\sigma_{ij}dv - \int_{\Gamma_c} N^A \boldsymbol{t} da\right)}{\partial u_k^B} = \int_{\Omega_c}\frac{\partial N^A}{\partial x_j}(J^{-1}F_{lN}F_{jM}\frac{\partial J[\boldsymbol{\sigma F}^{-T}]_{iM}}{\partial F_{kN}})\frac{\partial N^B}{\partial x_l}dv - \int_{\Gamma_c} N^A N^B \frac{\partial \boldsymbol{t}}{\partial u_k} da, \tag{A19}$$

with $[\quad]_{ij}$ represents the matrix component. We assume there is no surface traction, and thereby the last term in Eq. (A19) can be eliminated. Substitute Eq. (A6), and $\partial J[\boldsymbol{\sigma F}^{-T}]_{iM}/\partial F_{kN}$ can be expressed as

$$\frac{\partial J(\boldsymbol{\sigma F}^{-T})_{iM}}{\partial F_{kN}} = K_{iM,kN}^1 + K_{iM,kN}^2 + K_{iM,kN}^3 - K_{iM,kN}^4 + K_{iM,kN}^5 + K_{iM,kN}^6, \tag{A20}$$

where

$$K_{iM,kN}^1 = \partial\eta_0[\dot{\boldsymbol{\varepsilon}}\boldsymbol{F}^{-T}]_{iM}/\partial F_{kN}, \tag{A21}$$

$$K_{iM,kN}^2 = \partial\mu(l_\perp^{-1}[\boldsymbol{F l_0}]_{iM} - {F^{-1}}_{Mi})/\partial F_{kN}, \tag{A22}$$

$$K_{iM,kN}^3 = \partial\mu\left(l_\parallel^{-1} - l_\perp^{-1}\right)[\boldsymbol{Q F}^{-T}]_{iM}/\partial F_{kN}, \tag{A23}$$

$$K^4_{iM,kN} = \partial K[(\nabla \boldsymbol{d})^T \nabla \boldsymbol{d} \cdot \boldsymbol{F}^{-T}]_{iM}/\partial F_{kN}, \tag{A24}$$

$$K^5_{iM,kN} = \partial \eta_d [\boldsymbol{H}\boldsymbol{F}^{-T}]_{iM}/2\partial F_{kN}, \tag{A25}$$

$$K^6_{iM,kN} = \partial 2BJ(J-1){F^{-T}}_{Mi}/\partial F_{kN}, \tag{A26}$$

with tensor $\dot{\boldsymbol{\varepsilon}} = (\dot{\boldsymbol{F}}\boldsymbol{F}^{-1} + \boldsymbol{F}^{-T}\dot{\boldsymbol{F}}^T)/2$, $\boldsymbol{Q} = \boldsymbol{d} \otimes \boldsymbol{F}\widehat{\boldsymbol{l}_0}\boldsymbol{F}^T\boldsymbol{d}$, and $\boldsymbol{H} = \boldsymbol{d} \otimes \left(\dot{\boldsymbol{d}} - \boldsymbol{W}\boldsymbol{d}\right) - (\dot{\boldsymbol{d}} - \boldsymbol{W}\boldsymbol{d}) \otimes \boldsymbol{d}$. Therefore, $K^1_{iM,kN}$ to $K^6_{iM,kN}$ can be calculated as

$$K^1_{iM,kN} = \frac{\eta_0}{2}\Big(\frac{1}{\Delta t}[\boldsymbol{F}^{-1}\boldsymbol{F}^{-T}]_{NM}\delta_{ki} - [\dot{\boldsymbol{F}}\boldsymbol{F}^{-1}]_{ik}[\boldsymbol{F}^{-1}\boldsymbol{F}^{-T}]_{NM} + \frac{1}{\Delta t}F^{-1}_{Mk}F^{-1}_{Ni} - [\boldsymbol{F}^{-1}\dot{\boldsymbol{F}}\boldsymbol{F}^{-1}]_{Mk}F^{-1}_{Ni}\Big) - \eta_0[\dot{\boldsymbol{\varepsilon}}\boldsymbol{F}^{-T}]_{iN}F^{-1}_{Mk}, \tag{A27}$$

$$K^2_{iM,kN} = \mu l_\perp^{-1}\delta_{ki}{l_0}_{NM} + F^{-1}_{Ni}F^{-1}_{Mk}, \tag{A28}$$

$$K^3_{iM,kN} = \mu\left(l_\parallel^{-1} - l_\perp^{-1}\right)(D_{iN}F^{-1}_{Mk} + n_i[\boldsymbol{F}^{-1}\boldsymbol{F}\widehat{\boldsymbol{l}_0}]_{MN}n_k - [\boldsymbol{Q}\boldsymbol{F}^{-T}]_{iN}F^{-1}_{Mk}), \tag{A29}$$

$$K^4_{iM,kN} = -K([(\nabla \boldsymbol{d})^T \nabla \boldsymbol{d} \cdot \boldsymbol{F}^{-T}]_{kM}F^{-1}_{Ni} - [(\nabla \boldsymbol{d})^T \nabla \boldsymbol{d}]_{ki}[\boldsymbol{F}^{-1}\boldsymbol{F}^{-T}]_{MN} - [(\nabla \boldsymbol{d})^T \nabla \boldsymbol{d} \cdot \boldsymbol{F}^{-T}]_{iN}F^{-1}_{Mk}), \tag{A30}$$

$$K^5_{iM,kN} = \frac{\eta_d}{2}(-d_i\frac{\partial W_{ab}}{\partial F_{kN}}d_b + \frac{\partial W_{ib}}{\partial F_{kN}}d_b d_a)F^{-1}_{Ma} - \frac{\eta_d}{2}[\boldsymbol{H}\boldsymbol{F}^{-T}]_{iN}F^{-1}_{Mk}, \tag{A31}$$

$$K^6_{iM,kN} = 2BJ((2J-1)F^{-1}_{Nk}F^{-1}_{Mi} - (J-1)F^{-1}_{Ni}F^{-1}_{Mk}), \tag{A32}$$

where tensor $\boldsymbol{D} = \boldsymbol{d} \otimes \widehat{\boldsymbol{l}_0}\boldsymbol{F}^T\boldsymbol{d}$, Δt represents the time increment at each step, $\dot{\boldsymbol{d}} = (\boldsymbol{d}_{n+1} - \boldsymbol{d}_n)/\Delta t$ with variable $\boldsymbol{d}_{n+1}$ and $\boldsymbol{d}_n$ the directors at increment steps $n+1$ and n, respectively, and δ_{ki} represents Kronecker delta. $\partial W_{ab}/\partial F_{kn}$ in Eq. (A31) is

$$\frac{\partial W_{ab}}{\partial F_{kN}} = \frac{1}{2}(-[\dot{\boldsymbol{F}}\boldsymbol{F}^{-1}]_{ak}F^{-1}_{Nb} + [\dot{\boldsymbol{F}}\boldsymbol{F}^{-1}]_{bk}F^{-1}_{Na}) + \frac{1}{2\Delta t}(\delta_{ak}F^{-1}_{Nb} - \delta_{bk}F^{-1}_{Na}). \tag{A33}$$

To alleviate the convergent issue, following Chester et al. (Chester et al., 2015), we assume $\partial(\nabla \boldsymbol{d})/\partial \boldsymbol{F} = 0$ in deriving Eq. (A24), and approximate Eq. (A30) as

$$K^4_{iM,kN} = -K[(\nabla \boldsymbol{d})^T \nabla \boldsymbol{d} \cdot \boldsymbol{F}^{-T}]_{iN}F^{-1}_{Mk}). \tag{A34}$$

Similarly, the Jacobian stiffness $K^{AB}_{u_i\theta}$ is

$$K^{AB}_{u_i\theta} = \int_{\Omega_c}\frac{\partial N^A}{\partial x_j}\left(K^1_{ij,\theta} - K^2_{ij,\theta} + K^3_{ij,\theta}\right)N^B dv \tag{A35}$$

where

$$K^1_{ij,\theta} = \partial\mu\left(l_\parallel^{-1} - l_\perp^{-1}\right)Q_{ij}/\partial\theta \tag{A36}$$

$$K^2_{ij,\theta} = \partial[K(\nabla \boldsymbol{d})^T \nabla \boldsymbol{d}]_{ij}/\partial\theta, \tag{A37}$$

$$K_{ij,\theta}^{3} = \partial \eta_d H_{ij}/2\partial\theta, \tag{A38}$$

They can be calculated as:

$$K_{ij,\theta}^{1} = \mu\left(l_{\parallel}^{-1} - l_{\perp}^{-1}\right)[\frac{\partial d_i}{\partial \theta}[\boldsymbol{F}\widehat{\boldsymbol{l}_0}\boldsymbol{F}^{\boldsymbol{T}}\boldsymbol{d}]_j + d_i[\boldsymbol{F}\widehat{\boldsymbol{l}_0}\boldsymbol{F}^{\boldsymbol{T}}\frac{\partial \boldsymbol{d}}{\partial \theta}]_j], \tag{A39}$$

$$K_{ij,\theta}^{2} = K[\frac{\partial(\nabla \boldsymbol{d})^T}{\partial \theta}\nabla \mathbf{d} + (\nabla \boldsymbol{d})^T\frac{\partial \nabla \mathbf{d}}{\partial \theta}]_{ij}, \tag{A40}$$

$$K_{ij,\theta}^{3} = \frac{\eta_d}{2}(Z_{ij} - Z_{ji}), \tag{A41}$$

where tensor $\boldsymbol{Z} = \frac{\partial \boldsymbol{d}}{\partial \theta} \otimes \left(\dot{\boldsymbol{d}} - \boldsymbol{W}\boldsymbol{d}\right) + \boldsymbol{d} \otimes \left(\frac{\partial \dot{\boldsymbol{d}}}{\partial \theta} - \boldsymbol{W}\frac{\partial \boldsymbol{d}}{\partial \theta}\right)$, and $\partial \boldsymbol{d}/\partial\theta = (-\sin(\theta), \cos(\theta), 0)$.

The Jacobian stiffness $K_{\theta\theta}^{AB}$ is

$$K_{\theta\theta}^{AB} = \int_{\Omega_c}(N^A N^B\left(K_{\theta,\theta}^{1} + K_{\theta,\theta}^{3} - K_{\theta,\theta}^{4}\right) + \frac{\partial N^A}{\partial x}K_{\theta,\theta}^{2}\frac{\partial N^B}{\partial x})dv \tag{A42}$$

where $K_{\theta,\theta}^{1}$, $K_{\theta,\theta}^{2}$, $K_{\theta,\theta}^{3}$ and $K_{\theta,\theta}^{4}$ are:

$$K_{\theta,\theta}^{1} = \frac{\eta_d \partial \dot{\theta}}{\partial \theta} = \frac{\eta_d}{\Delta t}, \tag{A43}$$

$$K_{\theta,\theta}^{2} = K, \tag{A44}$$

$$K_{\theta,\theta}^{3} = \mu(l_{\parallel}^{-1} - l_{\perp}^{-1})S_{21}, \tag{A45}$$

$$K_{\theta,\theta}^{4} = \mu(l_{\parallel}^{-1} - l_{\perp}^{-1})S_{12}, \tag{A46}$$

with tensor $\boldsymbol{S} = \frac{\partial \boldsymbol{d}}{\partial \theta} \otimes \boldsymbol{F}\widehat{\boldsymbol{l}_0}\boldsymbol{F}^{\boldsymbol{T}}\boldsymbol{d} + \boldsymbol{d} \otimes \boldsymbol{F}\widehat{\boldsymbol{l}_0}\boldsymbol{F}^{\boldsymbol{T}}\frac{\partial \boldsymbol{d}}{\partial \theta}$.

The Jacobian stiffness $K_{\theta u_k}^{AB}$ is

$$K_{\theta u_k}^{AB} = \int_{\Omega_c} N^A\left(-K_{\theta,kN}^{1} + K_{\theta,kN}^{2} + K_{\theta,kN}^{3}\right)\frac{\partial N^B}{\partial x_a}F_{aN}dv, \tag{A47}$$

where the components $K_{\theta,kN}^{1}$, $K_{\theta,kN}^{2}$ and $K_{\theta,kN}^{3}$ are

$$K_{\theta,kN}^{1} = \mu\left(l_{\parallel}^{-1} - l_{\perp}^{-1}\right)[d_2\delta_{1k}[\widehat{\boldsymbol{l}_0}\boldsymbol{F}^{\boldsymbol{T}}\boldsymbol{d}]_N + d_2[\boldsymbol{F}\widehat{\boldsymbol{l}_0}]_{1N}d_k], \tag{A48}$$

$$K_{\theta,kN}^{2} = \mu\left(l_{\parallel}^{-1} - l_{\perp}^{-1}\right)[d_1\delta_{2k}[\widehat{\boldsymbol{l}_0}\boldsymbol{F}^{\boldsymbol{T}}\boldsymbol{d}]_N + d_1[\boldsymbol{F}\widehat{\boldsymbol{l}_0}]_{2N}d_k], \tag{A49}$$

$$K_{\theta,kN}^{3} = \frac{\eta_d}{2}([\dot{\boldsymbol{F}}\boldsymbol{F}^{-1}]_{2k}F_{N1}^{-1} - [\dot{\boldsymbol{F}}\boldsymbol{F}^{-1}]_{1k}F_{N2}^{-1} + \frac{1}{\Delta t}(\delta_{1k}F_{N2}^{-1} - \delta_{2k}F_{N1}^{-1})), \tag{A50}$$

To accommodate nearly incompressible solids and mitigate volumetric locking behavior, we implemented the F-bar method (Chester et al., 2015; de Souza Neto et al., 1996; Hughes, 1980). Based on the concept of splitting the deformation gradient into a volumetric part and a distortional part, we have

$$\boldsymbol{F} = \boldsymbol{F}_{dis}\boldsymbol{F}_{vol}, \tag{A51}$$

where $\boldsymbol{F}_{dis} = J^{-1/3}\boldsymbol{F}$ and $\boldsymbol{F}_{vol} = J^{1/3}\boldsymbol{I}$. The modified deformation gradient F-bar, $\overline{\boldsymbol{F}}$, is defined as the multiplication of the distortional part of $\boldsymbol{F}$ and the cubic root of the determinant of the deformation gradient $\boldsymbol{F}_{\boldsymbol{c}}$ at the centroid of each element

$$\overline{\boldsymbol{F}} = \left(\frac{\det(\boldsymbol{F}_{\boldsymbol{c}})}{J}\right)^{1/3}\boldsymbol{F}. \tag{A52}$$

It is clear that the distortional/volumetric split of $\overline{\boldsymbol{F}}$ is

$$\overline{\boldsymbol{F}} = \overline{\boldsymbol{F}}_{dis}\overline{\boldsymbol{F}}_{vol}, \tag{A53}$$

with $\overline{\boldsymbol{F}}_{dis} = \boldsymbol{F}_{dis}$ and $\overline{\boldsymbol{F}}_{vol} = (\boldsymbol{F}_{\boldsymbol{c}})_{vol}$. Thereby, the volumetric part changes to that at the centroid of the element, meaning that all the integration points in one element share the same volumetric deformation. We replace $\boldsymbol{F}$ by $\overline{\boldsymbol{F}}$ in the Cauchy stress Eq. (A6) so that the Cauchy stress at each Gauss point is computed as $\boldsymbol{\sigma}(\overline{\boldsymbol{F}})$. To simplify the implementation and calculation of the UEL, we still use $\boldsymbol{F}$ in Eq. (A7), but only applied $\overline{\boldsymbol{F}}$ to the residual equation related to the displacement, Eq. (A16). As a consequence, only the stiffness component $K^{AB}_{u_i u_k}$ needs to be modified to (Chester et al., 2015; de Souza Neto et al., 1996)

$$\overline{K^{AB}_{u_i u_k}} = K^{AB}_{u_i u_k} + \int \frac{\partial N^A}{\partial x_j}\boldsymbol{q}\left(\left(\frac{\partial N^B}{\partial x_l}\right)_c - \frac{\partial N^B}{\partial x_l}\right) dv, \tag{A54}$$

where $(\partial N^B/\partial x_l)_c$ is the gradient operator at the centroid of an element, and $\boldsymbol{q}$ is a fourth-order tensor defined by

$$\boldsymbol{q} = \frac{1}{2}\boldsymbol{A}\colon(\boldsymbol{I}\otimes\boldsymbol{I}) - \frac{1}{2}(\boldsymbol{\sigma}\otimes\boldsymbol{I}), \tag{A55}$$

with $A_{ijkl} = J^{-1}F_{lN}F_{jM}\frac{\partial J[\boldsymbol{\sigma}\boldsymbol{F}^{-T}]_{iM}}{\partial F_{kN}}$ the spatial elasticity tensor. The UEL and input files are available as separate Supplementary files.

Reference

Ahn, C., Liang, X., Cai, S., 2019. Bioinspired Design of Light-Powered Crawling, Squeezing, and Jumping Untethered Soft Robot. Adv. Mater. Technol. 4, 1900185. https://doi.org/10.1002/admt.201900185

Blaber, J., Adair, B., Antoniou, A., 2015. Ncorr: Open-Source 2D Digital Image Correlation Matlab Software. Exp. Mech. 55, 1105–1122. https://doi.org/10.1007/s11340-015-0009-1

Bladon, P., Terentjev, E.M., Warner, M., 1993. Transitions and instabilities in liquid crystal elastomers. Phys. Rev. E 47, R3838–R3840. https://doi.org/10.1103/PhysRevE.47.R3838

Broberg, K.B., 1999. Cracks and Fracture. Elsevier.

Chester, S.A., Di Leo, C.V., Anand, L., 2015. A finite element implementation of a coupled diffusion-deformation theory for elastomeric gels. Int. J. Solids Struct. 52, 1–18. https://doi.org/10.1016/j.ijsolstr.2014.08.015

Clarke, S.M., Terentjev, E.M., 1999. Slow stress relaxation in liquid crystal elastomers and gels. Faraday Discuss. 112, 325–333. https://doi.org/10.1039/a808847k

Courty, S., Miné, J., Tajbakhsh, A., Terentjev, E., 2003. Nematic elastomers with aligned carbon nanotubes: New electromechanical actuators. EPL Europhys. Lett. 64. https://doi.org/10.1209/epl/i2003-00277-9

de Souza Neto, E.A., Perić, D., Dutko, M., Owen, D.R.J., 1996. Design of simple low order finite elements for large strain analysis of nearly incompressible solids. Int. J. Solids Struct. 33, 3277–3296. https://doi.org/10.1016/0020-7683(95)00259-6

Ericksen, J.L., 1991. Liquid crystals with variable degree of orientation. Arch. Ration. Mech. Anal. 113, 97–120. https://doi.org/10.1007/BF00380413

Fan, W., Wang, Z., Cai, S., 2016. Rupture of Polydomain and Monodomain Liquid Crystal Elastomer. Int. J. Appl. Mech. 08, 1640001. https://doi.org/10.1142/S1758825116400019

Finkelmann, H., Nishikawa, E., Pereira, G.G., Warner, M., 2001. A New Opto-Mechanical Effect in Solids. Phys. Rev. Lett. 87, 015501. https://doi.org/10.1103/PhysRevLett.87.015501

Frank, F.C., 1958. I. Liquid crystals. On the theory of liquid crystals. Discuss. Faraday Soc. 25, 19–28. https://doi.org/10.1039/DF9582500019

Fukunaga, A., Urayama, K., Takigawa, T., DeSimone, A., Teresi, L., 2008. Dynamics of Electro-Opto-Mechanical Effects in Swollen Nematic Elastomers. Macromolecules 41, 9389–9396. https://doi.org/10.1021/ma801639j

Gasser, T.C., Ogden, R.W., Holzapfel, G.A., 2005. Hyperelastic modelling of arterial layers with distributed collagen fibre orientations. J. R. Soc. Interface 3, 15–35. https://doi.org/10.1098/rsif.2005.0073

He, X., Zheng, Y., He, Q., Cai, S., 2020. Uniaxial tension of a nematic elastomer with inclined mesogens. Extreme Mech. Lett. 40, 100936. https://doi.org/10.1016/j.eml.2020.100936

Higaki, H., Takigawa, T., Urayama, K., 2013. Nonuniform and Uniform Deformations of Stretched Nematic Elastomers. Macromolecules 46, 5223–5231. https://doi.org/10.1021/ma400771z

Hotta, A., Terentjev, E., 2001. Long-time stress relaxation in polyacrylate nematic liquid crystalline elastomers. J. Phys.-Condens. Matter 13, 11453–11464. https://doi.org/10.1088/0953-8984/13/50/305

Hughes, T.J.R., 1980. Generalization of selective integration procedures to anisotropic and nonlinear media. Int. J. Numer. Methods Eng. 15, 1413–1418. https://doi.org/10.1002/nme.1620150914

Jiang, Y., Jin, L., Huo, Y., 2021. Unusual stress and strain concentration behaviors at the circular hole of a large monodomain liquid crystal elastomer sheet. J. Mech. Phys. Solids 156, 104615. https://doi.org/10.1016/j.jmps.2021.104615

Jiang, Y., Li, D., Chen, Y., Huo, Y., 2023. Analysis of stress and strain concentration around a centralized elliptical hole in a monodomain liquid crystal elastomer sheet. Int. J. Solids Struct. 264, 112079. https://doi.org/10.1016/j.ijsolstr.2022.112079

Kaiser, A., Winkler, M., Krause, S., Finkelmann, H., M. Schmidt, A., 2009. Magnetoactive liquid crystal elastomer nanocomposites. J. Mater. Chem. 19, 538–543. https://doi.org/10.1039/B813120C

Kanninen, M.F., McEvily, A.J., Popelar, C.H., 1986. Advanced Fracture Mechanics. https://doi.org/10.1115/1.3225862

Knowles, J.K., Sternberg, E., 1974. Finite-deformation analysis of the elastostatic field near the tip of a crack: Reconsideration and higher-order results. J. Elast. 4, 201–233. https://doi.org/10.1007/BF00049265

Knowles, J.K., Sternberg, E., 1973. An asymptotic finite-deformation analysis of the elastostatic field near the tip of a crack. J. Elast. 3, 67–107. https://doi.org/10.1007/BF00045816

Kundler, I., Finkelmann, H., 1995. Strain-induced director reorientation in nematic liquid single crystal elastomers. Macromol. Rapid Commun. 16, 679–686. https://doi.org/10.1002/marc.1995.030160908

Küupfer, J., Finkelmann, H., 1994. Liquid crystal elastomers: Influence of the orientational distribution of the crosslinks on the phase behaviour and reorientation processes. Macromol. Chem. Phys. 195, 1353–1367. https://doi.org/10.1002/macp.1994.021950419

Lee, K.M., Smith, M.L., Koerner, H., Tabiryan, N., Vaia, R.A., Bunning, T.J., White, T.J., 2011. Photodriven, Flexural–Torsional Oscillation of Glassy Azobenzene Liquid Crystal Polymer Networks. Adv. Funct. Mater. 21, 2913–2918. https://doi.org/10.1002/adfm.201100333

Lehmann, W., Skupin, H., Tolksdorf, C., Gebhard, E., Zentel, R., Krüger, P., Lösche, M., Kremer, F., 2001. Giant lateral electrostriction in ferroelectric liquid-crystalline elastomers. Nature 410, 447–450. https://doi.org/10.1038/35068522

Leslie, F.M., 1992. Continuum theory for nematic liquid crystals. Contin. Mech. Thermodyn. 4, 167–175. https://doi.org/10.1007/BF01130288

Li, F.Z., Shih, C.F., Needleman, A., 1985. A comparison of methods for calculating energy release rates. Eng. Fract. Mech. 21, 405–421. https://doi.org/10.1016/0013-7944(85)90029-3

Lin, S., Zhou, Y., Zhao, X., 2014. Designing extremely resilient and tough hydrogels via delayed dissipation. Extreme Mech. Lett. 1, 70–75. https://doi.org/10.1016/j.eml.2014.11.002

Liu, M., Guo, J., Hui, C.-Y., Zehnder, A.T., 2019. Application of Digital Image Correlation (DIC) to the Measurement of Strain Concentration of a PVA Dual-Crosslink Hydrogel Under Large Deformation. Exp. Mech. 59, 1021–1032. https://doi.org/10.1007/s11340-019-00520-4

Long, R., Hui, C.-Y., 2015. Crack tip fields in soft elastic solids subjected to large quasi-static deformation — A review. Extreme Mech. Lett. 4, 131–155. https://doi.org/10.1016/j.eml.2015.06.002

Long, R., Hui, C.-Y., Gong, J.P., Bouchbinder, E., 2021. The Fracture of Highly Deformable Soft Materials: A Tale of Two Length Scales. Annu. Rev. Condens. Matter Phys. 12, 71–94. https://doi.org/10.1146/annurev-conmatphys-042020-023937

Lu, Y., Qi, Y., Tenardi, M., Long, R., 2021. Mixed-mode fracture in a soft elastomer. Extreme Mech. Lett. 48, 101380. https://doi.org/10.1016/j.eml.2021.101380

Luo, C., Chung, C., Yakacki, C.M., Long, K., Yu, K., 2022. Real-Time Alignment and Reorientation of Polymer Chains in Liquid Crystal Elastomers. ACS Appl. Mater. Interfaces 14, 1961–1972. https://doi.org/10.1021/acsami.1c20082

Mistry, D., B. Morgan, P., H. Clamp, J., F. Gleeson, H., 2018. New insights into the nature of semi-soft elasticity and "mechanical-Fréedericksz transitions" in liquid crystal elastomers. Soft Matter 14, 1301–1310. https://doi.org/10.1039/C7SM02107K

Naciri, J., Srinivasan, A., Jeon, H., Nikolov, N., Keller, P., Ratna, B.R., 2003. Nematic Elastomer Fiber Actuator. Macromolecules 36, 8499–8505. https://doi.org/10.1021/ma034921g

Okamoto, S., Sakurai, S., Urayama, K., 2021. Effect of stretching angle on the stress plateau behavior of main-chain liquid crystal elastomers. Soft Matter 17, 3128–3136. https://doi.org/10.1039/D0SM02244F

Peng, Z., Jiang, Y., Chen, Y., Huo, Y., 2023. Attenuating liquid crystal elastomers' stress concentration by programming initial orientation. Int. J. Mech. Sci. 249, 108274. https://doi.org/10.1016/j.ijmecsci.2023.108274

Qi, Y., Zou, Z., Xiao, J., Long, R., 2019. Mapping the nonlinear crack tip deformation field in soft elastomer with a particle tracking method. J. Mech. Phys. Solids 125, 326–346. https://doi.org/10.1016/j.jmps.2018.12.018

Rice, J.R., 1968. A Path Independent Integral and the Approximate Analysis of Strain Concentration by Notches and Cracks. J. Appl. Mech. 35, 379–386. https://doi.org/10.1115/1.3601206

Rivlin, R.S., Thomas, A.G., 1953. Rupture of rubber. I. Characteristic energy for tearing. J. Polym. Sci. 10, 291–318. https://doi.org/10.1002/pol.1953.120100303

Rogóż, M., Zeng, H., Xuan, C., Wiersma, D.S., Wasylczyk, P., 2016. Light-Driven Soft Robot Mimics Caterpillar Locomotion in Natural Scale. Adv. Opt. Mater. 4, 1689–1694. https://doi.org/10.1002/adom.201600503

Saed, M.O., Torbati, A.H., Nair, D.P., Yakacki, C.M., 2016. Synthesis of Programmable Main-chain Liquid-crystalline Elastomers Using a Two-stage Thiol-acrylate Reaction. JoVE J. Vis. Exp. e53546. https://doi.org/10.3791/53546

Sawa, Y., Urayama, K., Takigawa, T., DeSimone, A., Teresi, L., 2010. Thermally Driven Giant Bending of Liquid Crystal Elastomer Films with Hybrid Alignment. Macromolecules 43, 4362–4369. https://doi.org/10.1021/ma1003979

Schätzle, J., Kaufhold, W., Finkelmann, H., 1989. Nematic elastomers: The influence of external mechanical stress on the liquid-crystalline phase behavior. Makromol. Chem. 190, 3269–3284. https://doi.org/10.1002/macp.1989.021901224

Schuhladen, S., Preller, F., Rix, R., Petsch, S., Zentel, R., Zappe, H., 2014. Iris-Like Tunable Aperture Employing Liquid-Crystal Elastomers. Adv. Mater. 26, 7247–7251. https://doi.org/10.1002/adma.201402878

Stephen, M.J., Straley, J.P., 1974. Physics of liquid crystals. Rev. Mod. Phys. 46, 617–704. https://doi.org/10.1103/RevModPhys.46.617

Verwey, G.C., Warner, M., 1997. Compositional Fluctuations and Semisoftness in Nematic Elastomers. Macromolecules 30, 4189–4195. https://doi.org/10.1021/ma961801i

Verwey, G.C., Warner, M., Terentjev, E.M., 1996. Elastic Instability and Stripe Domains in Liquid Crystalline Elastomers. J. Phys. II 6, 1273–1290. https://doi.org/10.1051/jp2:1996130

Wang, C., Sim, K., Chen, J., Kim, H., Rao, Z., Li, Y., Chen, W., Song, J., Verduzco, R., Yu, C., 2018. Soft Ultrathin Electronics Innervated Adaptive Fully Soft Robots. Adv. Mater. 30, 1706695. https://doi.org/10.1002/adma.201706695

Warner, M., Terentjev, E.M., 2007. Liquid Crystal Elastomers. OUP Oxford.

Wei, C., Cao, S., Zhou, Y., Lin, D., Jin, L., 2023. Rate-dependent stress-order coupling in main-chain liquid crystal elastomers. Soft Matter. https://doi.org/10.1039/D3SM00770G

White, T.J., Broer, D.J., 2015. Programmable and adaptive mechanics with liquid crystal polymer networks and elastomers. Nat. Mater. 14, 1087–1098. https://doi.org/10.1038/nmat4433

White, T.J., Tabiryan, N.V., Serak, S.V., Hrozhyk, U.A., Tondiglia, V.P., Koerner, H., Vaia, R.A., Bunning, T.J., 2008. A high frequency photodriven polymer oscillator. Soft Matter 4, 1796–1798. https://doi.org/10.1039/B805434G

Winkler, M., Kaiser, A., Krause, S., Finkelmann, H., Schmidt, A.M., 2010. Liquid Crystal Elastomers with Magnetic Actuation. Macromol. Symp. 291–292, 186–192. https://doi.org/10.1002/masy.201050522

Wu, S., Hong, Y., Zhao, Y., Yin, J., Zhu, Y., 2023. Caterpillar-inspired soft crawling robot with distributed programmable thermal actuation. Sci. Adv. 9, eadf8014. https://doi.org/10.1126/sciadv.adf8014

Yu, Y., Ikeda, T., 2006. Soft Actuators Based on Liquid-Crystalline Elastomers. Angew. Chem. Int. Ed. 45, 5416–5418. https://doi.org/10.1002/anie.200601760

Yu, Y., Nakano, M., Ikeda, T., 2003. Directed bending of a polymer film by light. Nature 425, 145–145. https://doi.org/10.1038/425145a

Zhang, T., Lin, S., Yuk, H., Zhao, X., 2015. Predicting fracture energies and crack-tip fields of soft tough materials. Extreme Mech. Lett. 4, 1–8. https://doi.org/10.1016/j.eml.2015.07.007

Zhang, Y., Xuan, C., Jiang, Y., Huo, Y., 2019. Continuum mechanical modeling of liquid crystal elastomers as dissipative ordered solids. J. Mech. Phys. Solids 126, 285–303. https://doi.org/10.1016/j.jmps.2019.02.018